

Cu(InGa)Se₂ Solar Cells

William N. Shafarman¹ and Lars Stolt²

¹*University of Delaware, Newark, DE, USA,* ²*Uppsala University, Uppsala, Sweden*

13.1 INTRODUCTION

Cu(InGa)Se₂-based solar cells have often been touted as being among the most promising of solar cell technologies for cost-effective power generation. This is partly due to the advantages of thin films for low-cost, high-rate semiconductor deposition over large areas using layers only a few microns thick and for fabrication of monolithically interconnected modules. Perhaps more importantly, very high efficiencies have been demonstrated with Cu(InGa)Se₂ at both the cell and the module levels. Currently, the highest solar cell efficiency is 18.8% with 0.5 cm² total area fabricated by the National Renewable Energy Laboratory (NREL) [1]. Furthermore, several companies have demonstrated large area modules with efficiencies >12% including a confirmed 13.4% efficiency on a 3459 cm² module by Showa Shell [2]. Finally, Cu(InGa)Se₂ solar cells and modules have shown excellent long-term stability [3] in outdoor testing. In addition to its potential advantages for large-area terrestrial applications, Cu(InGa)Se₂ solar cells have shown high radiation resistance, compared to crystalline silicon solar cells [4, 5] and can be made very lightweight with flexible substrates, so they are also promising for space applications.

The history of CuInSe₂ solar cells starts with the work done at Bell Laboratories in the early 1970s, even though its synthesis and characterization were first reported by Hahn in 1953 [6] and, along with other ternary chalcopyrite materials, it had been characterized by several groups [7]. The Bell Labs group grew crystals of a wide selection of these materials and characterized their structural, electronic, and optical properties [7–9]. The first CuInSe₂ solar cells were made by evaporating *n*-type CdS onto *p*-type single crystals of CuInSe₂ [10]. These devices were initially recognized for their potential as near-infrared photodetectors since their spectral response was broader and more uniform than Si photodetectors. Optimization for solar cells increased the efficiency to 12% as measured under outdoor illumination “on a clear day in New Jersey” [11].

There has been relatively little effort devoted to devices on single-crystal CuInSe₂ since this early work, in part because of the difficulty in growing high-quality crystals [12]. Instead, nearly all the focus has gone to thin-film solar cells because of their inherent advantages. The first thin-film CuInSe₂/CdS devices were fabricated by Kazmerski *et al.* using films deposited by evaporation of CuInSe₂ powder along with excess Se [13]. However, thin-film CuInSe₂ solar cells began to receive a lot of attention when the first high-efficiency, 9.4%, cells were demonstrated by Boeing [14]. At the same time, interest in Cu₂S/CdS thin-film solar cells waned owing to problems related to electrochemical instabilities and many of these researchers turned their focus to CuInSe₂.

The Boeing devices were fabricated using CuInSe₂ deposited by coevaporation, that is, evaporation from separate elemental sources [15], onto ceramic substrates coated with a Mo back electrode. Devices were completed with evaporated CdS or (CdZn)S deposited in two layers with undoped CdS followed by an In-doped CdS layer that served as the main current-carrying material [15]. Throughout the 1980s, Boeing and ARCO Solar began to address the difficult manufacturing issues related to scale-up, yield, and throughput leading to many advancements in CuInSe₂ solar cell technology. The two groups pursued different approaches to CuInSe₂ deposition, which today remain the most common deposition methods and produce the highest device and module efficiencies. Boeing focused on depositing Cu(InGa)Se₂ by coevaporation, while ARCO Solar focused on a two-stage process of Cu and In deposition at a low temperature followed by a reactive anneal in H₂Se.

The basic solar cell configuration implemented by Boeing provided the basis for a series of improvements that have lead to the high-efficiency device technology of today. The most important of these improvements to the technology include the following:

- The absorber-layer band gap was increased from 1.02 eV for CuInSe₂ to 1.1–1.2 eV by the partial substitution of In with Ga, leading to a substantial increase in efficiency [16].
- The 1- to 2- μ m-thick doped (CdZn)S layer was replaced with a thin, ≤ 50 nm, undoped CdS and a conductive ZnO current-carrying layer [17]. This increased the cell current by increasing the short wavelength (blue) response.
- Soda lime glass replaced ceramic or borosilicate glass substrates. Initially, this change was made for the lower costs of the soda lime glass and its good thermal expansion match to CuInSe₂. However, it soon became clear that an increase in device performance and processing tolerance resulted primarily from the beneficial indiffusion of sodium from the glass [18].
- Advanced absorber fabrication processes were developed that incorporate band gap gradients that improve the operating voltage and current collection [19, 20].

From its earliest development, CuInSe₂ was considered promising for solar cells because of its favorable electronic and optical properties including its direct band gap with high absorption coefficient and inherent *p*-type conductivity. As science and technology developed, it also became apparent that it is a very forgiving material since (1) high-efficiency devices can be made with a wide tolerance to variations in Cu(InGa)Se₂ composition [21, 22], (2) grain boundaries are inherently passive so even films with grain sizes less than 1 μ m can be used, and (3) device behavior is insensitive to defects at the junction caused by a lattice mismatch or impurities between the Cu(InGa)Se₂ and

CdS. The latter enables high-efficiency devices to be processed despite exposure of the Cu(InGa)Se_2 to air prior to junction formation.

High-efficiency CuInSe_2 -based solar cells have been fabricated by at least 10 groups around the world. While these groups employ a variety of processing technologies, all the solar cells have the same basic cell structure built around a $\text{Cu(InGa)Se}_2/\text{CdS}$ junction in a substrate configuration with a Mo back contact. Figure 13.1 shows a cross-sectional schematic of a standard device. This structure utilizes a soda lime glass substrate, coated with a sputtered Mo layer as a back contact. After Cu(InGa)Se_2 deposition, the junction is formed by chemical bath–deposited CdS with thickness ≤ 50 nm. Then a high-resistance (HR) ZnO layer and a doped high-conductivity ZnO layer are deposited, usually by sputtering or chemical vapor deposition. Either a current-collecting grid or monolithic series interconnection completes the device or module, respectively. A TEM micrograph of the same structure, shown in Figure 13.2, clearly demonstrates the polycrystalline nature of these materials and the conformal coverage of the CdS layer.

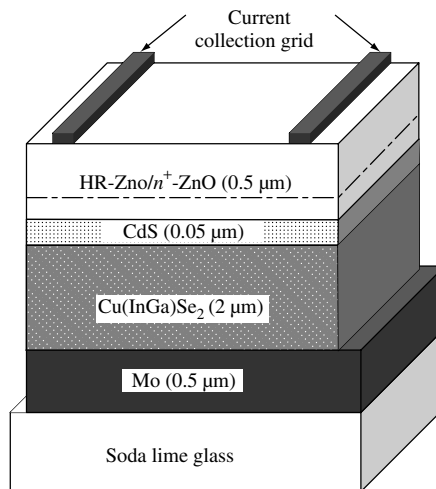


Figure 13.1 Schematic cross section of a typical Cu(InGa)Se_2 solar cell

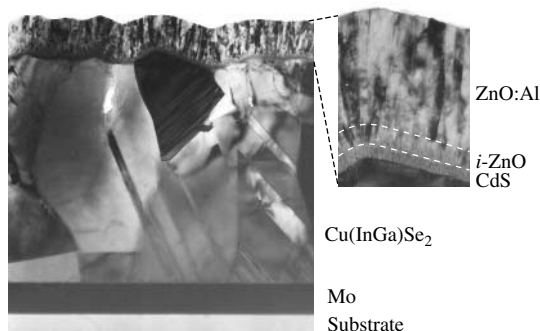


Figure 13.2 TEM cross section of a Cu(InGa)Se_2 solar cell

Several companies worldwide are pursuing the commercial development of Cu(InGa)Se₂-based modules. The most advanced, having demonstrated excellent reproducibility in its module manufacturing using the two-stage selenization process for Cu(InGa)(SeS)₂ deposition [3], is Shell Solar Industries (SSI) in California, which was formerly ARCO Solar and then Siemens Solar. They are now in production with 5-, 10-, 20-, and 40-W modules that are commercially available. In Germany, Würth Solar is in pilot production using an in-line coevaporation process for Cu(InGa)Se₂ deposition and has also reported large area modules with >12% efficiency. In the USA, several companies are in preproduction or pilot production: Energy Photovoltaics, Inc. (EPV) is using its own in-line evaporation process, International Solar Electric Technology (ISET) is developing a particle-based precursor for selenization, and Global Solar Energy (GSE) is pursuing a process for roll-to-roll coevaporation onto a flexible substrate. In Japan, Showa Shell, using a two-stage selenization process, and Matsushita, using coevaporation for Cu(InGa)Se₂ deposition, are also in production development stages.

Despite the level of effort on developing manufacturing processes, there remains a large discrepancy in efficiency between the laboratory-scale solar cells and minimodules, and the best full-scale modules. In part, this is due to the necessity for developing completely new processes and equipment for the large-area, high-throughput deposition needed for manufacturing thin-film photovoltaics. This is compounded by the lack of a comprehensive scientific base for Cu(InGa)Se₂ materials and devices, due partly to the fact that it has not attracted a broader interest for other applications. This lack of a science base has been perhaps the biggest hindrance to the maturation of Cu(InGa)Se₂ solar cell technology as most of the progress has been empirical. Still, in many areas a deeper understanding has emerged in the recent years.

In this chapter we will review the current status and the understanding of thin-film Cu(InGa)Se₂ solar cells from a technology perspective. For deeper scientific discussion of some aspects, we refer to suitable references. In order of presentation, this review covers (Section 13.2) structural, optical, and electrical properties of Cu(InGa)Se₂ including a discussion of the influence of Na and O impurities; (Section 13.3) methods used to deposit Cu(InGa)Se₂ thin films, the most common of which can be divided into two general types, multisource coevaporation and two-stage processes of precursor deposition followed by Se annealing; (Section 13.4) junction and device formation, which typically is done with chemical bath CdS deposition and a ZnO conduction layer; (Section 13.5) device operation with emphasis on the optical, current-collection, and recombination-loss mechanisms; (Section 13.6) module-manufacturing issues, including process and performance issues and a discussion of environmental concerns; and finally, (Section 13.7) a discussion of the outlook for CuInSe₂-based solar cells and critical issues for the future. In places where aspects of Cu(InGa)Se₂ solar cells cannot be covered in full, reference will be made to other review works that serve to complement this chapter.

13.2 MATERIAL PROPERTIES

The understanding of Cu(InGa)Se₂ thin films, as used in photovoltaic (PV) devices, is primarily based on studies of its base material, pure CuInSe₂. Thorough reviews on CuInSe₂ can be found in References [23–25]. However, the material used for making solar cells is Cu(InGa)Se₂ containing significant amounts (of the order of 0.1%) of Na [26].

Even though the behavior of CuInSe_2 provides a good basis for the understanding of device-quality material, there are pronounced differences when Ga and Na are present in the films. More recently, Cu(InGa)Se_2 has been reviewed in the context of solar cells with an emphasis on electronic properties [27].

In this section the structural, optical, and electrical properties of CuInSe_2 are reviewed along with information about the surface and grain boundaries and the effect of the substrate. In each case, as appropriate, the effect of the alloying with CuGaSe_2 to form Cu(InGa)Se_2 and the impact of Na and O on the material properties will be discussed.

13.2.1 Structure and Composition

CuInSe_2 and CuGaSe_2 have the chalcopyrite lattice structure. This is a diamond-like structure similar to the sphalerite structure but with an ordered substitution of the group I (Cu) and group III (In or Ga) elements on the group II (Zn) sites of sphalerite. This gives a tetragonal unit cell depicted in Figure 13.3 with a ratio of the tetragonal lattice parameters c/a close to 2 (see Table 13.1). The deviation from $c/a = 2$ is called the tetragonal distortion and stems from different strengths of the Cu–Se and the In–Se or Ga–Se bonds.

The possible phases in the Cu–In–Se system are indicated in the ternary phase diagram in Figure 13.4. Thin films of Cu–In–Se prepared under an excess supply of Se, that is, normal conditions for thin-film growth of Cu(InGa)Se_2 , have compositions that fall on, or close to, the tie-line between Cu_2Se and In_2Se_3 . Chalcopyrite CuInSe_2 is located on this line as well as a number of phases called ordered defect compounds (ODC), because they have a lattice structure described by the chalcopyrite structure with an ordered insertion of intrinsic defects. A comprehensive study of the Cu–In–Se phase diagram has been completed by Gödecke *et al.* [32]. A detail of the Cu_2Se – In_2Se_3 tie-line near CuInSe_2 is described by the pseudobinary phase diagram reproduced in Figure 13.5 [32]. Here α is the chalcopyrite CuInSe_2 , δ is a high-temperature (HT) phase with the sphalerite structure, and β is an ODC phase. It is interesting to note that the single phase field for CuInSe_2 at low temperatures is relatively narrow as compared to earlier beliefs, and does not contain

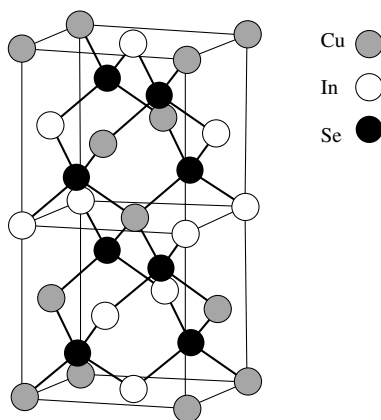
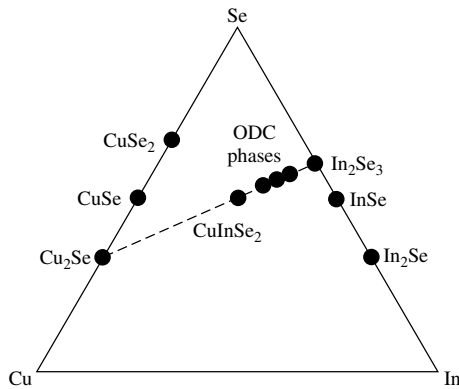


Figure 13.3 The unit cell of the chalcopyrite lattice structure

Table 13.1 Selected properties of CuInSe₂

Property		Value	Units	Reference
Lattice constant	a	5.78	Å	[28]
	c	11.62	Å	
Density		5.75	g/cm ³	[28]
Melting temperature		986	C	[29]
Thermal expansion coefficients at 273 K	(a axis)	8.32×10^{-6}	1/K	[30]
	(c axis)	7.89×10^{-6}	1/K	
Thermal conductivity at 273 K		0.086		[30]
Dielectric constant	Low frequency	13.6 ± 2.4		[31]
	High frequency	8.1 ± 1.4		
	Electrons	0.09		
Effective mass [m_e]	Holes (heavy)	0.71		[30]
	Holes (light)	0.092		[30]
Energy gap		1.02	eV	[30]
Energy gap temperature coefficient		-2×10^{-4}	eV/K	[30]

**Figure 13.4** Ternary phase diagram of the Cu–In–Se system. Thin-film composition is usually near the pseudobinary Cu₂Se–In₂Se₃ tie-line

the composition 25% Cu. At higher temperatures, around 500°C, where thin films are grown, the phase field widens toward the In-rich side. Typical average compositions of device-quality films have 22 to 24 at.% Cu, which fall within the single-phase region at growth temperature.

CuInSe₂ can be alloyed in any proportion with CuGaSe₂, thus forming Cu(InGa)Se₂. Similarly, the binary phase In₂Se₃ at the end point of the pseudobinary tie-line can be alloyed to form (InGa)₂Se₃, although it undergoes a structural change at Ga/(In + Ga) = 0.6 [33]. In high-performance devices, Ga/(In + Ga) ratios are typically 0.2 to 0.3.

One of the central characteristics of Cu(InGa)Se₂ is its ability to accommodate large variations in composition without appreciable differences in optoelectronic properties.

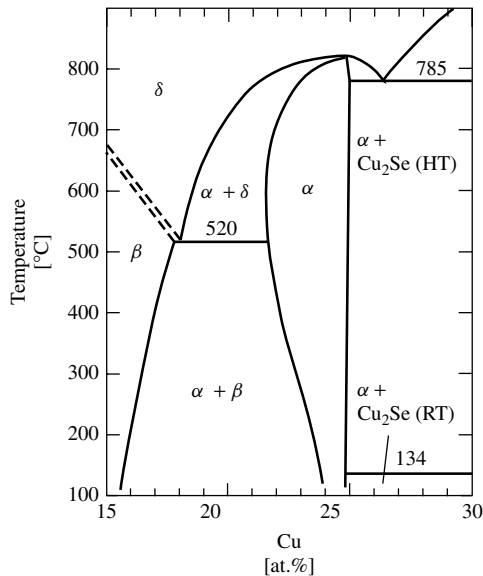


Figure 13.5 Pseudobinary In_2Se_3 – Cu_2Se equilibrium phase diagram for compositions around the CuInSe_2 chalcopyrite phase, denoted α . The δ phase is the high-temperature sphalerite phase, and the β phase is an ordered defect phase (ODC). Cu_2Se exists as a room-temperature (RT) or high-temperature (HT) phase. (After Gödecke T, Haalboom T, Ernst F, *Z. Metallkd.* **91**, 622–634 (2000) [32])

This tolerance is one of the cornerstones of the potential of $\text{Cu}(\text{InGa})\text{Se}_2$ as a material for efficient low-cost PV modules. Solar cells with high performance can be fabricated with $\text{Cu}/(\text{In} + \text{Ga})$ ratios from 0.7 to nearly 1.0. This property can be understood from theoretical calculations that show that the defect complex $2V_{\text{Cu}} + \text{In}_{\text{Cu}}$, that is, two Cu vacancies with an In on Cu antisite defect, has very low formation energy, and also that it is expected to be electrically inactive [34]. Thus, the creation of such defect complexes can compensate for Cu-poor/In-rich compositions of CuInSe_2 without adverse effects on the photovoltaic performance. Furthermore, crystallographic ordering of this defect complex is predicted [34], which explains the observed ODC phases $\text{Cu}_2\text{In}_4\text{Se}_7$, CuIn_3Se_5 , CuIn_5Se_8 , and so on.

The chalcopyrite phase field is increased by the addition of Ga or Na [35]. This can be explained by a reduced tendency to form the ordered defect compounds owing to higher formation energy for Ga_{Cu} (in CuGaSe_2) than for In_{Cu} (in CuInSe_2). This leads to destabilization of the $2V_{\text{Cu}} + \text{In}_{\text{Cu}}$ defect cluster related to the ODC phases [36, 37]. The effect of Na in the CuInSe_2 structure has been calculated by Wei *et al.* [38], with the result that Na replaces In_{Cu} antisite defects, reducing the density of compensating donors. This theoretical result is supported by measurements of epitaxial $\text{Cu}(\text{InGa})\text{Se}_2$ films in which Na is found to strongly reduce the concentration of compensating donors [37]. Together with a tendency for Na to occupy Cu vacancies, the reduced tendency to form antisite defects also suppresses the formation of the ordered defect compounds. The calculated effect of Na is therefore consistent with the experimental observations of increased compositional range in which single-phase chalcopyrite exists and increased conductivity [38, 39].

13.2.2 Optical Properties

The absorption coefficient α for CuInSe₂ is very high, larger than $10^5/\text{cm}$ for 1.4 eV and higher photon energies [40]. In many studies it was found that the fundamental absorption edge is well described by [30]

$$\alpha = A(E - E_g)^2/E \quad (13.1)$$

as for a typical direct band gap semiconductor. The proportionality constant A depends on the density of states associated with the photon absorption. From this relation, a band gap value of $E_g = 1.02 \pm 0.02$ eV is obtained. The temperature dependence follows

$$E_g(T) = E_g(0) - aT^2/(b + T) \quad (13.2)$$

where a and b are constants that vary between different measurements. In general, dE_g/dT is about -2×10^{-4} eV/K [41].

A rather complete picture of the optical properties of CuInSe₂ and other Cu-ternary chalcopyrites is given in Reference [42]. Ellipsometric measurements of carefully prepared single-crystal samples were carried out and the dielectric functions were obtained together with the complex refractive index for different polarizations. From these measurements a band gap value for CuInSe₂ of 1.04 eV was determined.

A similar study was also made on bulk polycrystalline ingots of Cu(InGa)Se₂ having different compositions from $x \equiv \text{Ga}/(\text{Ga} + \text{In}) = 0$ to 1 [43]. Curves describing the complex refractive index, $n + ik$, for samples with $x = 0$ and 0.2 are reproduced in Figure 13.6. The complex refractive index can be used to calculate other optical parameters like the absorption coefficient

$$\alpha = 4\pi k/\lambda \quad (13.3)$$

In the same work the fundamental transitions for the different compositions were fit to an equation describing the band gap for CuIn_{1-x}Ga_xSe₂ as

$$E_g = 1.010 + 0.626x - 0.167x(1 - x) \quad (13.4)$$

In this equation the so-called bowing coefficient is 0.167. A value of 0.21 was obtained by theoretical calculations as compared to values in the range of 0.11 to 0.26 determined in various experiments [44].

13.2.3 Electrical Properties

CuInSe₂ with an excess of Cu is always p -type but In-rich films can be made p -type or n -type [45]. By annealing in a selenium overpressure, n -type material can be converted to p -type, and conversely, by annealing in a low selenium pressure, p -type material becomes n -type [46]. It is believed that this affects the concentration of Se vacancies, V_{Se} , which act as compensating donors in p -type films. Device-quality Cu(InGa)Se₂ films, grown with the excess Se available, are p -type with a carrier concentration of about $10^{16}/\text{cm}^3$.

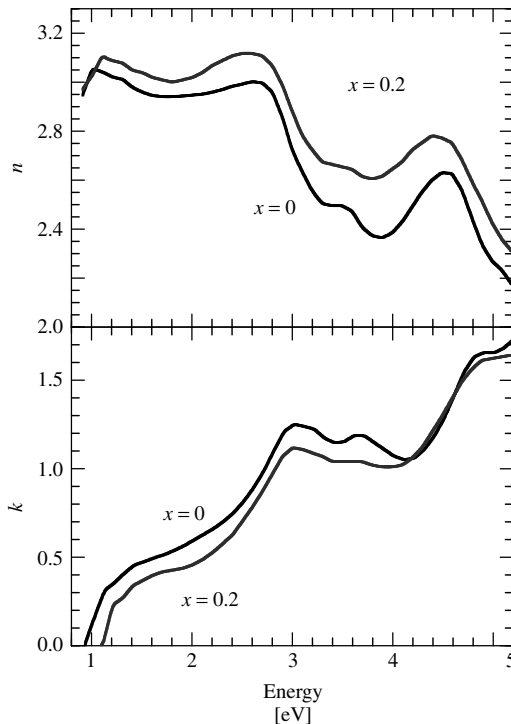


Figure 13.6 Complex refractive index for CuInSe_2 and $\text{CuIn}_{1-x}\text{Ga}_x\text{Se}_2$ with $x = 0.2$ (After Alonso M *et al.*, *Appl. Phys. A* **74**, 659–664 (2002) [43])

There is a large spread in mobility values reported for CuInSe_2 . The highest values of hole mobilities have been obtained for epitaxial films, where $200 \text{ cm}^2/\text{Vs}$ has been measured for $\text{Cu}(\text{InGa})\text{Se}_2$ with about $10^{17}/\text{cm}^3$ in hole concentration [37]. Single crystals have yielded values in the range of 15 to $150 \text{ cm}^2/\text{Vs}$. Electron mobilities determined from single crystals range from 90 to $900 \text{ cm}^2/\text{Vs}$ [46]. Conductivity and Hall effect measurements of thin-film samples are made cross-grain, but for device operation through-the-grain values are more relevant, since individual grains may extend from the back contact to the interface of the junction. The sheet conductivities of polycrystalline *p*-type films correspond to mobility values of 5 to $50 \text{ cm}^2/\text{Vs}$, but it is quite possible that they are limited by transport across grain boundaries.

A large number of intrinsic defects are possible in the chalcopyrite structure. Accordingly, a number of electronic transitions have been observed by methods such as photoluminescence, photoconductivity, photovoltage, optical absorption, and electrical measurements (see, for example, Reference [31]). However, it is difficult to assign transitions to specific defects on an experimental basis. Instead, theoretical calculations of the transition energies and formation energies provide a basis for identification of the different intrinsic defects that are active in $\text{Cu}(\text{InGa})\text{Se}_2$. Calculations of intrinsic defects in CuInSe_2 and comparison with experimental data can be found in the comprehensive paper by Zhang *et al.* [47]. A summary of their results is schematically shown in Figure 13.7. The defects that are considered most important in device-quality material are presented in Table 13.2.

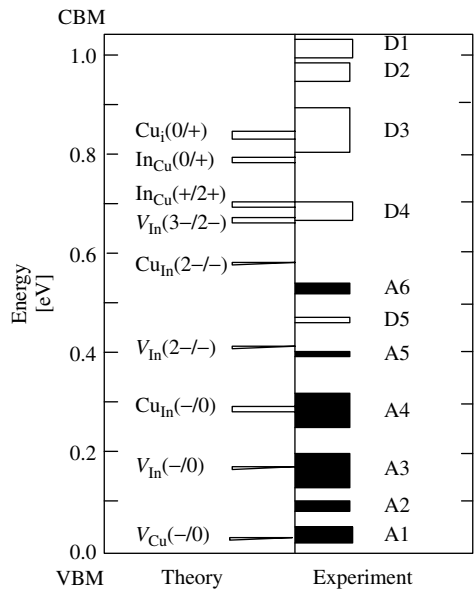


Figure 13.7 Electronic levels of intrinsic defects in CuInSe₂. On the left side the theoretical values are presented and on the right side experimentally reported values are presented. The height of the histogram columns on the right side represents the spread in experimental data. (From Zhang S, Wei S, Zunger A, Katayama-Yoshida H, *Phys. Rev. B* **57**, 9642–9656 (1998) [47])

Table 13.2 The most important intrinsic defects for device-quality CuInSe₂

Defect	Energy position	Type
V_{Cu}	$E_{\text{V}} + 0.03 \text{ eV}$	Shallow acceptor
In_{Cu}	$E_{\text{C}} - 0.25 \text{ eV}$	Compensating donor
V_{Se}		Compensating donor
Cu_{In}	$E_{\text{V}} + 0.29 \text{ eV}$	Recombination center

The effect of Ga on the electronic and defect properties is discussed in Reference [36]. In those calculations, acceptor levels did not differ very much between CuInSe₂ and CuGaSe₂, but the donor levels are deeper in the Ga-containing compound. This is consistent with observations of increased *p*-type conductivity at high Ga-concentrations [48]. At typical device compositions, $\text{Ga}/(\text{Ga} + \text{In}) < 0.3$, any effect of increased Ga content on conductivity has not been verified.

13.2.4 The Surface and Grain Boundaries

The surface morphology and grain structure are most commonly characterized by scanning electron microscopy (SEM), but transmission electron microscopy (TEM) and atomic force microscopy have also proved valuable. A typical SEM image is shown in Figure 13.8 and a TEM cross-sectional image in Figure 13.2. In general, the films used in devices

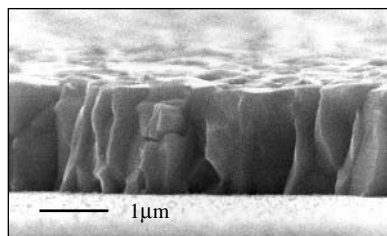


Figure 13.8 Scanning electron microscopy image of a typical Cu(InGa)Se₂ film deposited on a Mo-coated glass substrate by coevaporation

have grain diameters on the order of 1 μm but the grain size and morphology can vary greatly depending on fabrication method and conditions. A variety of defects including twins, dislocations, and stacking faults have been observed [49–51].

It has been shown by X-ray photoelectron spectroscopy (XPS) that the free surfaces of CuInSe₂ films with slightly Cu-poor composition have a composition close to CuIn₃Se₅ [52], corresponding to one of the ordered defect phases. Many attempts have been made to identify such a layer on top of the films without success. It merely seems as if the composition gradually changes from the bulk to the surface of the films. It was proposed by Herberholz *et al.* [35] that band bending induced by surface charges drives electromigrating Cu into the bulk leaving the surface depleted of Cu. This depletion is stopped when the composition is that of CuIn₃Se₅, since further depletion requires a structural change of the material. Electromigration of Cu in CuInSe₂ has been demonstrated and also correlated with type conversion of the chalcopyrite material [53].

The band bending as well as the CuIn₃Se₅ composition of CuInSe₂ surfaces disappears when the material is exposed to atmosphere for some time as oxides form on the surface. The surface oxidation is enhanced by the presence of Na [39]. The surface compounds after oxidation have been identified as In₂O₃, Ga₂O₃, SeO_x, and Na₂CO₃ [54]. A review of the surface and the interface properties can be found in Reference [55].

It has been common practice to posttreat Cu(InGa)Se₂ devices in air at typically 200°C. When devices were fabricated using vacuum-evaporated CdS or (CdZn)S to form the junction, these anneals were often done for several hours to optimize the device performance [14, 56]. The main effect associated with oxygen is explained as passivation of selenium “surface” vacancies on the grains [57]. The V_{Se} at the grain boundaries can act as a recombination center. The positive charge associated with these donor-type defects reduces the effective hole concentration at the same time that the intergrain carrier transport is impeded. When oxygen substitutes for the missing selenium, these negative effects are canceled.

The overall noted beneficial effect of the presence of Na on the PV performance of Cu(InGa)Se₂ thin films lacks a complete explanation. In Reference [58] it is proposed that the catalytic effect of Na on oxidation, by enhanced dissociation of molecular oxygen into atomic oxygen, makes the passivation of V_{Se} on grain surfaces more effective. This model is consistent with the observation that Na and O are predominantly found at the grain boundaries rather than in the bulk of the grains in CuInSe₂ thin films [59].

13.2.5 Substrate Effects

The effects of the substrate on the properties of thin-film polycrystalline Cu(InGa)Se₂ can be classified into three categories: (1) thermal expansion, (2) chemical effects, and (3) surface influence on nucleation.

It can be assumed that after growth, when the substrate and film are still at the growth temperature, the stress in the Cu(InGa)Se₂ film is low. The cooling down from growth temperature imposes a temperature change of about 500°C, and if the thermal expansion of the substrate and Cu(InGa)Se₂ is different stress will be built up in the film. The thermal expansion coefficient for CuInSe₂ is around $9 \times 10^{-6}/\text{K}$ in the temperature interval of interest, which is similar to that of soda lime glass. A CuInSe₂ film deposited on a substrate with a lower thermal expansion coefficient, such as borosilicate glass, will be under increasing tensile stress during cooldown. Typically, such films exhibit voids and microcracks [50]. When the thermal expansion coefficient of the substrate is higher than that of the film material, like for polyimide, it will result in compressive stress in the thin-film material, which may lead to adhesion failures.

The most important effect of the soda lime glass substrate on Cu(InGa)Se₂ film growth is that it supplies sodium to the growing chalcopyrite material. It has been clearly shown that this effect is distinct from the thermal expansion match of soda lime glass [60]. The sodium diffuses through the Mo back contact, which also means that it is important to control the properties of the Mo [61]. The resulting microstructure of Cu(InGa)Se₂ is clearly influenced by the presence of Na with larger grains and a higher degree of preferred orientation, with the (112) axis perpendicular to the substrate. An explanation for this effect when high concentrations of Na are present has been proposed by Wei *et al.* [38].

There is a wide range of preferred orientation between different growth processes, in spite of similar device performance. One reason for this variation is most likely the different properties of the surfaces on which the chalcopyrite material nucleates. A comparison between Cu(InGa)Se₂ grown on normal Mo-coated substrates and directly on soda lime glass shows that a much more pronounced (112) orientation occurs on glass, in spite of no difference in the Na concentration, as measured in the films afterwards [18]. Further, the preferred orientation of the Cu(InGa)Se₂ film has been shown to be correlated to the orientation of the Mo film [62] or an (InGa)₂Se₃ precursor layer [63].

13.3 DEPOSITION METHODS

A wide variety of thin-film deposition methods has been used to deposit Cu(InGa)Se₂ thin films. To determine the most promising technique for the commercial manufacture of modules, the overriding criteria are that the deposition can be completed at low cost while maintaining high deposition or processing rate with high yield and reproducibility. Compositional uniformity over large areas is critical for high yield. Device considerations dictate that the Cu(InGa)Se₂ layer should be at least 1 μm thick and that the relative compositions of the constituents are kept within the bounds determined by the phase diagram, as discussed in Section 13.2.1. For solar cell or module fabrication, the Cu(InGa)Se₂ is most commonly deposited on a molybdenum-coated glass substrate,

though other substrate materials including metal or plastic foils have also been used and may have processing advantages.

The most promising deposition methods for the commercial manufacture of modules can be divided into two general approaches that have both been used to demonstrate high device efficiencies and in pilot scale manufacturing. The first approach is vacuum coevaporation in which all the constituents, Cu, In, Ga, and Se, can be simultaneously delivered to a substrate heated to 400 to 600°C and the Cu(InGa)Se₂ film is formed in a single growth process. This is usually achieved by thermal evaporation from elemental sources at temperatures greater than 1000°C for Cu, In, and Ga. The second approach is a two-step process that separates the delivery of the metals from the reaction to form device-quality films. Typically the Cu, Ga, and In are deposited using low-cost and low-temperature methods that facilitate uniform composition. Then the films are annealed in a Se atmosphere, also at 400 to 600°C. The reaction and anneal step often takes longer time than formation of films by coevaporation due to diffusion kinetics, but is amenable to batch processing. High process rate can be achieved by moving continuously through sequential process steps or with a batch process whereby longer deposition or reaction steps can be implemented by handling many substrates in parallel.

13.3.1 Substrates

Soda lime glass, which is used in conventional windows, is the most common substrate material used for Cu(InGa)Se₂ since it is available in large quantities at low cost and has been used to make the highest efficiency devices. Cu(InGa)Se₂ deposition requires a substrate temperature (T_{SS}) of at least 350°C and the highest efficiency cells have been fabricated using films deposited at the maximum temperature, $T_{SS} \approx 550^\circ\text{C}$, which the glass substrate can withstand without softening too much [64]. The glass is electrically insulating and smooth, which enables monolithic integration into modules.

The soda lime glass has a thermal expansion coefficient of $9 \times 10^{-6}/\text{K}$ [64], which provides a good match to the Cu(InGa)Se₂ films. The glass composition typically includes various oxides such as Na₂O, K₂O, and CaO. These provide sources of alkali impurities that diffuse into the Mo and Cu(InGa)Se₂ films during processing [18], producing the beneficial effects discussed in Section 13.2. However, a process that provides a more controllable supply of Na than diffusion from the glass substrate is preferred. This can be achieved by blocking sodium from the substrate with a diffusion barrier such as SiO_x or Al₂O₃. Then sodium can be directly provided to the Cu(InGa)Se₂ growth process by depositing a sodium-containing precursor layer onto the Mo film [65, 66]. Commercially available soda lime glass may also contain significant structural defects that can adversely impact module production [67]. Borosilicate glass does not contain the alkali impurities and may have fewer structural imperfections but has a lower thermal expansion coefficient, $4.6 \times 10^{-6}/\text{K}$ [64], and is more expensive.

Substrates such as metal or plastic foils have advantages over glass substrates owing to their light weight and flexibility, which will be discussed in Section 13.6. Cu(InGa)Se₂ devices have been demonstrated with different metal and high-temperature polyimide substrates [68, 69].

13.3.2 Back Contact

The Mo back contact, used for all high-efficiency devices, is typically deposited by direct current (dc) sputtering. The thickness is determined by the resistance requirements that depend on the specific cell or module configuration. A film with thickness 1 μm will typically have a sheet resistance of 0.1 to 0.2 Ω/\square , a factor of 2 to 4 higher resistivity than bulk Mo. Sputter deposition of the Mo layer requires careful control of the pressure to control stress in the film [70] and to prevent problems such as poor adhesion that it might cause. During Cu(InGa)Se₂ deposition, a MoSe₂ layer forms at the interface [71]. Its properties are influenced by the Mo film with less MoSe₂ forming on dense Mo, sputter-deposited under low pressures [51]. This interfacial layer does not necessarily degrade device performance. Metals other than Mo have been investigated with limited success [72].

13.3.3 Coevaporation of Cu(InGa)Se₂

The highest efficiency devices have been deposited by thermal coevaporation from elemental sources [73]. An illustration of a laboratory system for Cu(InGa)Se₂ coevaporation is shown in Figure 13.9. The process uses line-of-sight delivery of the Cu, In, Ga, and Se from Knudsen-type effusion cells or open-boat sources to the heated substrate. While the evaporation temperatures for each metal will depend on the specific source design, typical ranges are 1300 to 1400°C for Cu, 1000 to 1100°C for In, 1150 to 1250°C for Ga, and 300 to 350°C for Se evaporation.

The sticking coefficients of Cu, In, and Ga are very high, so the film composition and growth rate are determined simply by the flux distribution and effusion rate from each source. The composition of the final film tends to follow the pseudobinary tie-line between (InGa)₂Se₃ and Cu₂Se (see Figure 13.4) according to the relative concentration of Cu compared to In and Ga. The relative concentrations of In and Ga determine the band gap of the film, according to equation (13.4), and the effusion rates can be varied over the course of a deposition to change the film composition through its thickness. Se has a

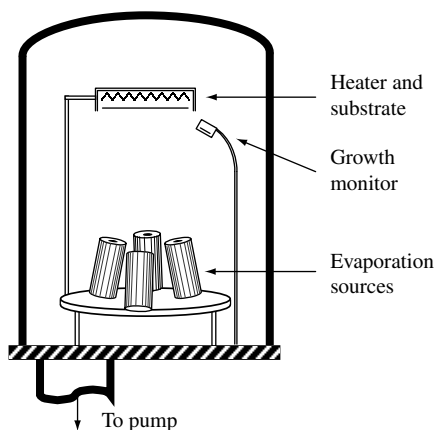


Figure 13.9 Configuration for multisource elemental coevaporation

much higher vapor pressure and lower sticking coefficient, so it is always evaporated in excess of that needed in the final film. Insufficient Se can result in a loss of In and Ga in the form of In_2Se or Ga_2Se [74].

Different deposition variations, using elemental fluxes deliberately varied over time, have been explored using coevaporation. Four different sequences that have been used to fabricate devices with efficiencies greater than 16% are shown in Figure 13.10. In each case, the targeted final composition is Cu-deficient with $\text{Cu}/(\text{In} + \text{Ga}) = 0.8 - 0.9$. The total deposition time may vary from 10 to 90 min, depending on the effusion rates from the sources. So, for a film thickness of 2 μm , typical deposition rates vary from 20 to 200 nm/min.

The first process is the simplest stationary process in which all fluxes are constant throughout the deposition process [75]. In most cases, however, the fluxes are varied using what is referred to as the Boeing process in which the bulk of the film is grown with Cu-rich overall composition so that it contains a Cu_xSe phase in addition to $\text{Cu}(\text{InGa})\text{Se}_2$ [15]. The fluxes are then adjusted to finish the deposition with In- and Ga-rich flux so that the final film composition has the desired Cu-deficient composition. One modification of this is the second process shown in Figure 13.10. This process was first implemented with CuInSe_2 films deposited on non-Na containing substrates at $T_{\text{SS}} = 450^\circ\text{C}$, producing films with increased grain size and improved device performance. The effect of Cu_xSe as a flux for enhanced grain growth at higher T_{SS} was proposed by Klenk *et al.* [76]. However, in devices containing Na and Ga and with $T_{\text{SS}} > 500^\circ\text{C}$, no difference was found in the device performance using films with Cu-rich or uniform growth processes [75].

The third process shown in Figure 13.10 is a sequential process in which the In and Ga are deposited separately from the Cu. This was first proposed by Kessler *et al.* [77] with the deposition of an $(\text{InGa})_x\text{Se}_y$ compound, followed by the deposition of Cu and Se until the growing film reaches the desired composition. The layers interdiffuse to form the $\text{Cu}(\text{InGa})\text{Se}_2$ film. A modification by Gabor *et al.* [78] allows the Cu delivery to continue until the film has an overall Cu-rich composition. Then a third step is added to the process in which In and Ga, again in the presence of excess Se, are evaporated to bring the composition back to Cu-deficient. The metals interdiffuse, forming the ternary chalcopyrite film. This process has been used to produce the highest efficiency devices [1]. The improved device performance has been attributed to a band gap gradient, which results from the Ga concentration decreasing from the Mo back contact to the film's free surface [19], and to improved crystallinity of the films [79].

The last process shown in Figure 13.10 is an in-line process in which the flux distribution results from the substrate moving sequentially over the Cu, Ga, and In sources. This was first simulated in a stationary evaporation system [80] and has subsequently been implemented by several groups in pilot manufacturing systems (see Section 13.6).

A reproducible coevaporation process requires good control of the elemental fluxes from each evaporation source. While the evaporation rates from each source can be controlled simply by the source temperature, this may not give good reproducibility, especially for the Cu source that is at the highest temperature. Open-boat sources in particular will not give reproducible evaporation rates. Consequently, direct *in situ* measurement of the fluxes is often used to control the evaporation sources. Electron impact spectroscopy [15], quadrupole mass spectroscopy [81], and atomic absorption spectroscopy [82] have all

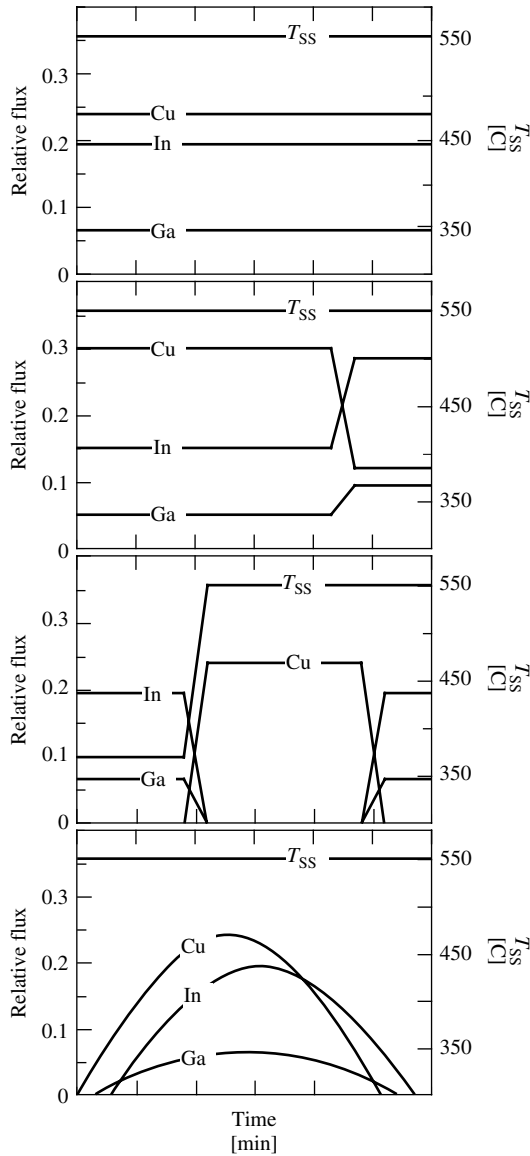


Figure 13.10 Relative metal fluxes and substrate temperature for different coevaporation processes. In all cases, a constant Se flux is also supplied

been successfully implemented. Direct flux measurement may be critical in a manufacturing scale process, particularly if source depletion over long run times causes the relation between source temperature and effusion rate to vary over time. In addition, the process can be monitored by *in situ* film thickness measurement using a quartz crystal monitor, or optical spectroscopy or X-ray fluorescence of the growing film [83]. The latter has also been used to measure composition. When the process includes a transition from Cu-rich to Cu-poor composition near the end of the deposition, it can be monitored by a change

in the temperature resulting from a change in the emissivity of the film [84] or by the infrared transmission [85].

The primary advantage of elemental coevaporation for depositing Cu(InGa)Se_2 films is its considerable flexibility to choose the process specifics and to control film composition and band gap. As proof of this flexibility, high-efficiency devices have been demonstrated using many process variations. The primary disadvantage results from the difficulty in control, particularly of the Cu-evaporation source, and the resulting need for improved deposition, diagnostic, and control technology. A second disadvantage is the lack of commercially available equipment for large-area thermal evaporation.

13.3.4 Two-step Processes

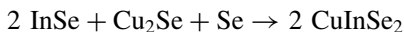
The second common approach to Cu(InGa)Se_2 film formation, usually referred to as two-step processing or selenization, has many variations in both the precursor deposition and the Se reaction steps. This general approach was first demonstrated by Grindle *et al.* [86] who sputtered Cu/In layers and reacted them in hydrogen sulfide to form CuInS_2 . This was first adapted to CuInSe_2 by Chu *et al.* [87]. The highest-efficiency Cu(InGa)Se_2 cell reported using the reaction in H_2Se is 16.2%, on the basis of the active area [88], but there has been less effort at optimizing laboratory-scale cell efficiencies than with coevaporated Cu(InGa)Se_2 . Showa Shell and Shell Solar have successfully scaled up this process to pilot commercial production and have demonstrated large-area module efficiencies as high as 13.4% [2].

The metal precursor is used to determine the final composition of the film and to ensure spatial uniformity. Sputtering is an attractive process because it is easily scalable using commercially available deposition equipment and can provide good uniformity over large areas with high deposition rates. However, other processes may have lower cost. CuInSe_2 has been formed using metal precursor layers deposited by electrodeposition [89], thermal or electron beam evaporation [90], screen printing [91], and application of nanoparticles [92]. Precursors that include Se, such as stacked layers of Cu/In/Se [93] or binary selenides, have also been used as precursor materials in various sequences and combinations [94]. Electrodeposition [95, 96] of Cu, In, Ga, and Se is effectively just another option for precursor deposition since the films similarly require a selenium reaction step.

The precursor films are typically reacted in either H_2Se or Se vapor at 400 to 500°C for 30 to 60 min to form the best device quality material. Poor adhesion [89] and formation of a MoSe_2 layer [97] at the Mo/ CuInSe_2 interface may limit the reaction time and temperature. Reaction in H_2Se has the advantage that it can be done at atmospheric pressure and can be precisely controlled, but the gas is highly toxic and requires special precautions for its use. The precursor films can also be reacted in a Se vapor, which might be obtained by thermal evaporation, to form the CuInSe_2 film [98]. A third reaction approach is rapid thermal processing (RTP) of either elemental layers, including Se, [99, 100] or amorphous evaporated Cu–In–Se layers [101].

The reaction chemistry and kinetics for the conversion of Cu–In precursors to CuInSe_2 has been characterized by X-ray diffraction of time-progressive reactions [102] and by *in situ* differential scanning calorimetry [103]. The results of these experiments

describe CuInSe₂ formation as a sequence of reactions starting with the formation of Cu₁₁In₉ and In liquid, which will contain a small concentration of dissolved Cu. These react with Se to form a series of binary compounds. The formation of CuInSe₂ then follows from



with complete reaction in ~ 15 min at 400°C. The reaction path was shown to be the same for the reaction of Cu/In layers in either H₂Se or elemental Se [104].

The addition of Ga, regardless of the precursor deposition sequence, does not readily give a film with uniformly increased band gap. Instead, all Ga in the reacted film accumulates near the Mo forming a CuInSe₂/CuGaSe₂ structure, so the resulting device behaves like CuInSe₂ [105] and lacks the increased operating voltage and other benefits of a wider band gap discussed in Section 13.5.4. Nevertheless, Ga inclusion provides improved adhesion of the CuInSe₂ film to the Mo back contact and greater device performance, possibly owing to an improved structure with fewer defects [105]. The Ga and In can be effectively interdiffused, converting the films to uniform band gap, by annealing in an inert atmosphere for 1 h at 600°C [106]. This anneal, however, may be impractical for commercial processing, so films in the best devices have the band gap increased by the incorporation of S near the front surface, forming a graded Cu(InGa)(SeS)₂ layer [20, 107] that can give enhanced operating voltage in devices.

The primary advantages of two-step processes for Cu(InGa)Se₂ deposition are the ability to utilize more standard and well-established techniques for the metal deposition and reaction and anneal steps and to compensate for long reaction times with a batch processing mode or RTP of Se-containing precursors. Composition and uniformity are controlled by the precursor deposition and can be measured between the two steps. The biggest drawback to these processes is the limited ability to control composition and increase band gap, which may limit device and module performance. Other difficulties that must be overcome include poor adhesion and the use of hydrogen selenide, which is hazardous and costly to handle.

13.3.5 Other Deposition Approaches

CuInSe₂-based films have been deposited using a wide range of thin-film deposition methods, in addition to those discussed above, which have been proposed as potential low-cost alternatives for manufacturing. These include reactive sputtering [108], hybrid sputtering in which Cu, In, and Ga are sputtered while Se is evaporated [109], closed-space sublimation [110], chemical bath deposition (CBD) [111], laser evaporation [112], and spray pyrolysis [113]. Great effort was made to explore different thin-film deposition techniques before coevaporation and the two-step processes above became dominant. These methods are reviewed in Reference [25].

13.4 JUNCTION AND DEVICE FORMATION

The first experimental device that indicated the potential for CuInSe₂ in high-performance solar cells was a heterojunction between a *p*-type single crystal of CuInSe₂ and a thin film of *n*-type CdS [10, 11]. Consequently, in the early thin-film work the junction was

formed by depositing CdS on the CuInSe₂ films [114]. The device was further developed to contain an undoped layer of CdS, followed by CdS doped with In, both deposited by vacuum evaporation [14]. This defined the device structure (see Figure 13.1), which is basically the same as is commonly used today since the doped CdS is functionally a transparent conductor. A performance gain was achieved by alloying the CdS with ZnS to widen the band gap [15]. Further improvement of the performance was achieved when the doped CdS layer was replaced with doped ZnO [115, 116]. The undoped CdS layer adjacent to the Cu(InGa)Se₂ film was reduced in thickness in order to maximize the optical transmission. Since ZnO has a wider band gap than CdS, more light is transmitted into the active part of the device, resulting in a current gain. A conformal and pinhole-free coating of this thin CdS layer is obtained by using chemical bath deposition to make the CdS buffer layer.

13.4.1 Chemical Bath Deposition

Chemical bath deposition (CBD) of thin-film materials can be viewed as a chemical vapor deposition (CVD) in the liquid phase instead of the gas phase. It is also referred to as solution growth. The method has been used in particular for chalcogenide materials such as PbS [117], CdS [118], and CdSe [119]. A variety of precursor compounds or ions can be used to deposit a specific compound.

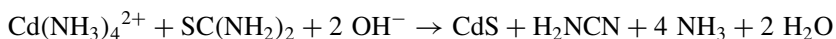
Deposition of CdS buffer layers on Cu(InGa)Se₂ is generally made in an alkaline aqueous solution (pH > 9) of the following three constituents:

1. a cadmium salt; for example, CdSO₄, CdCl₂, CdI₂, Cd(CH₃COO)₂
2. a complexing agent; commonly NH₃ (ammonia)
3. a sulfur precursor; commonly SC(NH₂)₂ (thiourea).

The concentrations of the various components of the solution can be varied over a range and each laboratory tends to use its own specific recipe. One example of a recipe that is being used to fabricate state-of-the-art Cu(InGa)Se₂ solar cells is

1. 1.4×10^{-3} M CdI₂ or CdSO₄
2. 1 M NH₃
3. 0.14 M SC(NH₂)₂

The Cu(InGa)Se₂ film is immersed in a bath containing the solution and the deposition takes place in a few minutes at a temperature of 60 to 80°C. This can be done either by immersion in a room-temperature bath that subsequently is heated to the desired temperature or by preheating the solution. The reaction proceeds according to the formula



In practice, the chemical bath deposition is typically done in the laboratory with a very simple apparatus consisting of a hot plate with magnetic stirring, a beaker holding the solutions into which the substrate is immersed, and a thermocouple to measure bath

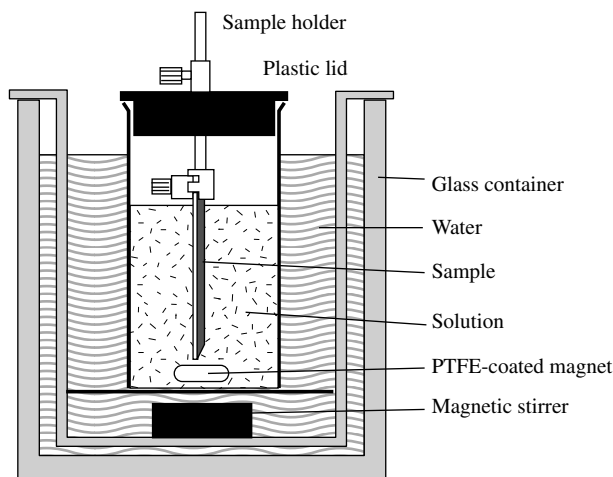


Figure 13.11 Typical laboratory apparatus for chemical bath deposition of CdS

temperature. A typical arrangement, incorporating a water bath for more uniform temperature, is shown in Figure 13.11. Scale-up of the CBD process for manufacturing will be discussed in Section 13.6.1.

The growth of CdS thin films by CBD occurs from ion by ion reaction or by clustering of colloidal particles. Depending on the bath condition, the resulting CdS lattice structure may be cubic, hexagonal, or a mixture [120]. Under typical conditions used for Cu(InGa)Se₂ solar cells, the relatively thin CdS layers grow ion by ion, resulting in dense homogeneous films [121] with mixed cubic/hexagonal or predominantly hexagonal lattice structure [51, 122, 123]. The films consist of crystallites with a grain size of the order of tens of nanometers [122].

Compositional deviation from stoichiometry is commonly observed. In particular, films tend to be sulfur-deficient and contain substantial amounts of oxygen [124, 125]. In addition to oxygen, significant concentrations of hydrogen, carbon, and nitrogen have also been detected in device quality films [126]. The concentration of these impurities has been correlated to a reduction of the optical band gap and the amount of cubic CdS in relation to hexagonal CdS [127].

13.4.2 Interface Effects

The interface between the Cu(InGa)Se₂ and the CdS is characterized by pseudoepitaxial growth of the CdS and intermixing of the chemical species. Electronic band alignment will be discussed in Section 13.5.3. Transmission electron microscopy has shown that chemical bath-deposited CdS layers on Cu(InGa)Se₂ films exhibit an epitaxial relationship at the interface with (112) chalcopyrite Cu(InGa)Se₂ planes parallel to the (111) cubic or (002) hexagonal CdS planes [51, 123]. The lattice mismatch is very small for pure CuInSe₂ with a (112) spacing of 0.334 nm as compared to a spacing of 0.336 nm for (111) cubic and (002) hexagonal CdS. In Cu(InGa)Se₂ the lattice mismatch increases with the Ga content. CuIn_{0.7}Ga_{0.3}Se₂ and CuIn_{0.5}Ga_{0.5}Se₂ have (112) spacing of 0.331 nm

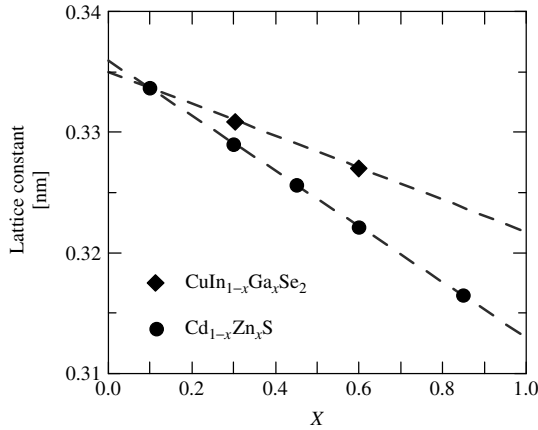


Figure 13.12 The lattice spacing of the (112) planes of $\text{CuIn}_{1-x}\text{Ga}_x\text{Se}_2$ and the (111) cubic or the (002) hexagonal planes of $\text{Cd}_{1-x}\text{Zn}_x\text{S}$. Empirical data from References [128] ((CdZn)S) and [129] (CuInSe_2 , CuGaSe_2 , and $(\text{Cu}(\text{InGa})\text{Se}_2)$) are included

and 0.328 nm, respectively. Figure 13.12 displays the (112) spacing for $\text{Cu}(\text{InGa})\text{Se}_2$ as a function of Ga/(In + Ga) ratio together with the (111)/(002) spacing of CdS–ZnS alloys.

When $\text{Cu}(\text{InGa})\text{Se}_2$ films are immersed in the chemical bath for deposition of CdS, they are also subjected to chemical etching of the surface. In particular, native oxides are removed by the ammonia [130]. Thus, the CBD process cleans the $\text{Cu}(\text{InGa})\text{Se}_2$ surface and enables the epitaxial growth of the CdS buffer layer.

In early single-crystal work, *p*–*n* homojunction diodes were fabricated by indiffusion of Cd or Zn into *p*-type CuInSe_2 [131, 132] at 200 to 450°C. Investigations of $\text{CuInSe}_2/\text{CdS}$ interfaces did show interdiffusion of S and Se above 150°C and rapid Cd diffusion into CuInSe_2 above 350°C [133]. More recently, intermixing of the constituents of the $\text{Cu}(\text{InGa})\text{Se}_2/\text{CdS}$ heterojunction has been observed even when the relatively low-temperature CBD process is used for growth of the CdS layer [134]. Investigations of the effect of a chemical bath without the thiourea showed an accumulation of Cd on the $\text{Cu}(\text{InGa})\text{Se}_2$ surface, possibly as CdSe [130]. Accumulation of Cd on the $\text{Cu}(\text{InGa})\text{Se}_2$ surface was also observed in the initial stage of CdS growth in the complete chemical bath [135]. The results were not conclusive on whether any interfacial compound is formed, but TEM investigations showed the presence of Cd up to 10 nm into the Cu-deficient surface region of the $\text{Cu}(\text{InGa})\text{Se}_2$ layer [123]. At the same time, a reduction of the Cu concentration was noted. An interpretation in which Cu^+ is replaced with Cd^{2+} is proposed, on the basis of the very close ion radii of these ions, 0.96 and 0.97, respectively. XPS and secondary ion mass spectrometry (SIMS) profiles of $\text{Cu}(\text{InGa})\text{Se}_2$ films and CuInSe_2 single crystals exposed to chemical baths without thiourea also show evidence of indiffusion or electromigration of Cd [136].

13.4.3 Other Deposition Methods

In the early days of $\text{Cu}(\text{InGa})\text{Se}_2$ research, vacuum evaporation of 2 to 3- μm -thick CdS was the standard method to fabricate the junction and 9.4% efficiency was obtained with

pure CuInSe₂ absorbers [14]. With evaporation it is difficult to nucleate and grow very thin continuous CdS layers such as those normally used in current state-of-the-art Cu(InGa)Se₂ devices, and the optical transmission of the window will be limited to energies less than the CdS band gap, 2.4 eV. Substrate temperatures of 150 to 200°C are used to obtain good optical and electrical properties of the evaporated CdS films. This is substantially higher than the substrate temperature used for chemical bath deposition. Improved device performance was achieved by alloying the evaporated CdS with ZnS [15]. Mixed (CdZn)S has a wider band gap, allowing increased optical transmission, and better lattice match to Cu(InGa)Se₂ than CdS.

The main drawback with vacuum evaporation is poor conformal coating resulting in nonuniform and incomplete coverage of the sometimes relatively rough Cu(InGa)Se₂ films. Sputter deposition leads to more conformal coverage. The general success of sputtering for industrial large-area deposition motivated the exploration of sputter-deposited CdS buffer layers. Using optical emission spectroscopy to control the sputtering process, Cu(InGa)Se₂ devices with efficiencies up to 12.1% were fabricated, as compared to 12.9% for reference cells with chemical bath-deposited CdS [137]. Both evaporation and sputtering are vacuum processes, which can be incorporated in-line with other vacuum processing steps and do not create any liquid wastes. Still, CBD remains the preferred process for the CdS layer owing to its advantages in forming thin conformal coatings.

Atomic layer chemical vapor deposition (ALCVD) is a method that also allows accurate control of the growth of thin conformal layers [138]. The method is being industrially used for deposition of another II-VI compound, ZnS. Inorganic precursors for deposition of CdS require the substrate temperature to be excessively high (>300°C) and work with organic precursors has been limited. The strong driving force for replacement of the environmentally undesirable cadmium has focused the development of ALCVD on materials other than CdS. This is also valid for regular CVD, although some metal organic CVD (MOCVD) work has been reported. The full potential for chemical vapor-deposited CdS has therefore not been explored.

Electrodeposition can be used to deposit CdS films but its use has not been reported in Cu(InGa)Se₂ devices.

13.4.4 Alternative Buffer Layers

The cadmium content in Cu(InGa)Se₂ PV modules with CBD CdS buffer layers is low. Investigations show that the cadmium in Cu(InGa)Se₂ modules can be handled safely, both with respect to environmental concerns and hazards during manufacturing (see Section 13.6.5). In spite of this, it would be preferable to eliminate cadmium in new products. There are in principle two approaches to Cd-free devices: (1) finding a buffer material that replaces CdS and (2) omitting the CdS layer and depositing ZnO directly onto the Cu(InGa)Se₂ film. In practice, the two approaches tend to merge when the chemical bath deposition of CdS is replaced with a surface treatment of the Cu(InGa)Se₂ with no or negligible film deposition before the subsequent deposition of the ZnO.

A number of approaches and materials have been tried. A selection of promising results are presented in Table 13.3.

Table 13.3 Performance of Cu(InGa)Se₂ thin-film solar cells with various buffer layers and junction-formation methods alternative to chemical bath deposition of CdS

Buffer material	Deposition method	Efficiency [%]	V _{OC} [mV]	J _{SC} [mA/cm ²]	FF [%]	Reference
None		10.5 ^a	398	39.0	68	[139]
None		15.0 ^b	604	36.2	69	[1]
ZnO	MOCVD	13.9 ^a	581	34.5	69	[140]
ZnO	ALCVD	11.7	512	32.6	70	[141]
Zn treatment	ZnCl ₂ solution	14.2 ^b	558	36.3	70	[142]
Zn(O,S,OH) _x	Chemical bath	14.2 ^{c,d}	567 ^e	36.6 ^e	68	[143]
ZnS	Chemical bath	16.9 ^{a,b}	647	35.2	74	[144]
Zn treatment + ZnS	Chemical bath + ILGAR ^f	14.2	559	35.9	71	[145]
Zn(Se,OH)	Chemical bath	13.7 ^{b,d}	535	36.1	71	[146]
ZnSe	ALCVD	11.6 ^a	502	35.2	65	[147]
ZnSe	MOCVD	11.6	469	35.8	69	[148]
In _x Se _y	Coevaporation	13.0 ^a	595	30.4	72	[149]
ZnIn _x Se _y	Coevaporation	15.1	652	30.4	76	[150]
In _x (OH,S) _y	Chemical bath	15.7 ^{a,b}	594	35.5	75	[151]
In ₂ S ₃	ALCVD	13.5	604	30.6	73	[152]

^aActive area^bWith antireflection layer^cMinimodule^dConfirmed^eRecalculated to single-cell values^fIon Layer Gas Reaction

When the numbers in Table 13.3 are analyzed, one must keep in mind that the quality of the Cu(InGa)Se₂ layer varies significantly between the experiments. For example, in the early results with direct ZnO [139], the reference cells with chemical bath-deposited CdS showed 12.4% efficiency, whereas the 15% efficiency results [1] are obtained from Cu(InGa)Se₂, which at best yielded an efficiency of 18.8%. On the other hand, an inferior junction-formation method may cause a larger degradation of cell efficiency at higher efficiency levels, since its defects may be relatively more important to the cell performance. In order to evaluate the various Cd-free junction-formation methods from that respect, the efficiency from each experiment is displayed in Figure 13.13 together with its reference, or estimation thereof. In most cases, the Cd-free device is comparable to the CBD-CdS device within typical variations.

Altogether, it appears as if there are several possibilities for obtaining high efficiency without Cd. All the listed methods include one or more of the elements Zn, In, and S. Zn is directly included in most of the buffer materials or indirectly as ZnO transparent contact with In_xSe_y, In(OH,S)_x, and In₂Se₃. Indications that *n*-type doping with Zn occurs similarly to that with Cd have been found by the treatment of Cu(InGa)Se₂ in Cd and Zn solutions [136], and are consistent with junction formation by solid-state diffusion into single crystals [132].

In Figure 13.13 a slight tendency can be noted toward larger difference between Cd-free and CdS reference cells for the direct ZnO approaches. It appears as if a buffer layer between the Cu(InGa)Se₂ and the ZnO is beneficial. Such a layer could passivate the

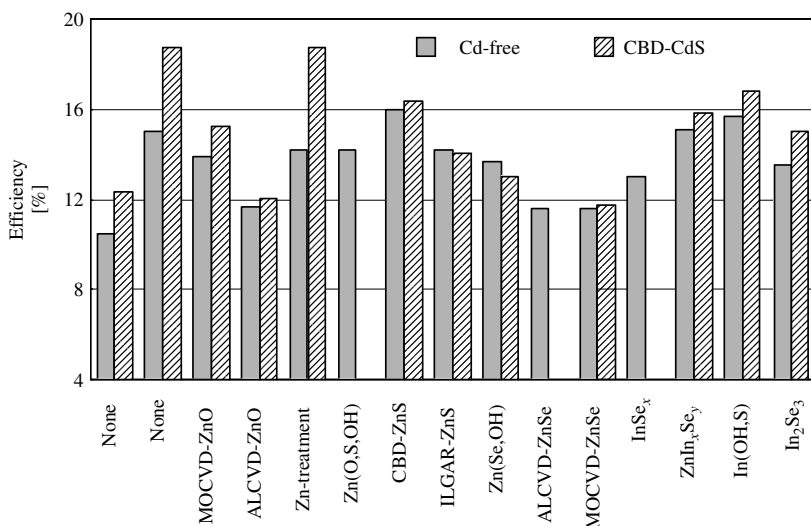


Figure 13.13 The efficiency of Cu(InGa)Se₂ solar cells with a selection of Cd-free junction-formation methods together with corresponding values of Cu(InGa)Se₂ cells with chemical bath-deposited CdS

Cu(InGa)Se₂ surface, which would reduce the recombination in a shallow *n*-type emitter, and possibly also serve to protect the junction and near-surface region during subsequent deposition of the transparent contact materials.

13.4.5 Transparent Contacts

The early Cu(InGa)Se₂ devices used CdS doped with In or Ga as front-contact layers in addition to the CdS buffer layer. Short wavelength light (<520 nm) was absorbed near the surface in the thick CdS layer and did not generate any photocurrent. When chemical bath deposition allowed CdS buffer layers to be thin enough such that it no longer limited the short wavelength collection in the Cu(InGa)Se₂, photocurrent could be gained by increasing the band gap of the contact layer. Since the contact layer must also have high conductivity for lateral current collection, the obvious choice is a transparent conducting oxide (TCO), a class of materials used in such devices as displays and low-emission coatings on window glass panes. There are three main materials in this class: SnO₂, In₂O₃:Sn (ITO), and ZnO. SnO₂ requires relatively high deposition temperatures that restrict the potential in Cu(InGa)Se₂ devices that cannot withstand temperatures greater than 200 to 250°C after CdS is deposited. ITO and ZnO can both be used, but the most common material is ZnO, favored by potentially lower material costs. A good overview of TCO thin-film materials can be found in Reference [153].

The most commonly used low-temperature deposition method for TCO films is sputtering. ITO layers are routinely fabricated on an industrial scale using dc sputtering. Industrial practice is to use ceramic ITO targets and to sputter in an Ar:O₂ mixture. Typical sputter rates range between 0.1 to 10 nm/s, depending on the application [154].

Sputtering of doped ZnO films is not as developed as is sputtering of ITO. Nevertheless, it is the preferred method for depositing the transparent front contact on Cu(InGa)Se₂

devices, with and without CBD–CdS, in the majority of the R&D groups. Typically, ZnO:Al films are deposited by radio frequency (rf) magnetron sputtering from ceramic ZnO:Al₂O₃ targets with 1 or 2 weight% Al₂O₃. In large-scale manufacturing, dc sputtering from ceramic targets is favored since it requires simpler equipment and offers higher deposition rates [155].

Reactive dc sputtering from Al/Zn alloy targets has also been used in the fabrication of Cu(InGa)Se₂/CdS devices with the same performance as with rf sputtered ZnO:Al [156]. The use of Zn/Al alloy targets allows lower costs than ceramic ZnO:Al₂O₃ targets, but reactive sputtering requires very precise process control owing to the so-called hysteresis effect [157] so that optimal optoelectronic properties are achieved only within a very narrow process window. Deposition rates in 4 to 5 nm/s range have been achieved.

Chemical vapor deposition (CVD) provides another deposition option and is used by one commercial manufacturer of Cu(InGa)Se₂ modules to deposit ZnO [158]. The reaction occurs at atmospheric pressure between water vapor and diethylzinc and the films are doped with fluorine or boron.

ALCVD deposition of ZnO has also been tested [159]. The atomic layer by atomic layer growth gives very low deposition rates, but the surface-controlled growth process gives uniform layers within a wide process window concerning reactant flow. This allows large batches to be processed, resulting in a reasonable throughput in spite of the limited growth rate.

As with the Mo back contact, the requirements for sheet resistance of the transparent contact layer will depend on the specific cell or module design. Typically, small area cells use layers with 20–30 Ω/\square , while modules may require 5–10 Ω/\square . In either case, the sheet resistance is usually controlled by the layer thickness.

13.4.6 Buffer Layers

It is common practice to use a buffer layer of undoped high-resistivity (HR) ZnO before sputter deposition of the TCO layer. Depending on the deposition method and conditions, this layer may have a resistivity of 1–100 $\Omega\text{ cm}$ compared to the transparent contact with 10^{-4} – 10^{-3} $\Omega\text{ cm}$. Typically, 50 nm of HR ZnO is deposited by rf magnetron sputtering from an oxide target.

The gain in performance by using an HR ZnO buffer layer in ordinary devices with CBD–CdS is related to the CdS thickness [156, 160, 161]. One explanation of the role of a ZnO buffer layer is given by [160] as resulting from locally nonuniform electronic quality of the Cu(InGa)Se₂ layer that can be modeled by a parallel diode with high recombination current. The influence of these regions on the overall performance is reduced by the series resistance of the HR ZnO layer. This series resistance has a negligible effect on the performance of the dominant parts of the device area. A related explanation would attribute the local areas with poor diode characteristics caused by pinholes in the CdS layer, which create parallel diodes with a Cu(InGa)Se₂/ZnO junction. In this case improved diode quality due to the ZnO buffer would improve overall performance. Either case is consistent with the observation that a beneficial effect from the ZnO buffer is not observed when the CBD–CdS layer is thick enough [161].

Another potential reason for using an HR ZnO buffer layer is to add protection of the interface region from sputter damage induced during deposition of the TCO layer which typically requires more harsh conditions. This seems to be particularly important for some alternative Cd-free buffer layers or with dc magnetron–sputtered TCO layers [162].

13.4.7 Device Completion

In order to contact laboratory test cells, a metal contact is deposited onto the TCO layer. It is shaped as a grid with minimum shadow area in order to allow as much light as possible into the device. Solar cell measurement standards recommend a minimum cell area of 1 cm², but many labs routinely use cells in the order of 0.5 cm². The metal grid contact can be made by first depositing some tens of nanometers of Ni to prevent the formation of a high resistance oxide layer, and subsequently depositing a few micrometers of Al. Evaporation through an aperture mask is a suitable deposition method.

After deposition of the metal grid, the total cell area is defined by removing the layers on top of the Mo outside the cell area by mechanical scribing or laser patterning. Alternatively, just the layers on top of the Cu(InGa)Se₂ can be removed, by photolithography and etching, since the lateral resistance of the Cu(InGa)Se₂ prevents collection outside the cell area.

The only significant difference in the device layers between lab cells and modules is the thickness of the TCO. Modules normally do not have any grid that assists in current collection over the cell area, so a substantially thicker TCO layer, that is, higher sheet conductivity, is needed in order to keep resistive losses low. A TCO layer with higher sheet conductivity may also have lower optical transmission in the infrared due to increased free-carrier absorption resulting in a decreased photocurrent.

13.5 DEVICE OPERATION

Cu(InGa)Se₂ solar cells have achieved efficiencies approaching 20%, the highest of any thin-film solar cells, largely by empirical processing improvements and in spite of relatively poor understanding of the underlying mechanisms and electronic defects that control the device behavior. However, a more complete picture of the device operation is emerging to enable both a better understanding of the devices and identification of pathways to further improvements.

The operation of Cu(InGa)Se₂/CdS solar cells is characterized by high quantum efficiency (QE) and short-circuit current. The open-circuit voltage increases with the band gap of the absorber layer and is insensitive to grain boundaries and defects at the Cu(InGa)Se₂/CdS interface. A basic device model can be constructed in which the voltage is limited by recombination through bulk trap states in the space charge region of the Cu(InGa)Se₂ absorber layer. Recombination at the Cu(InGa)Se₂/CdS interface is minimized by proper doping and band alignment or surface treatment to create an effective n -type inversion layer in the near-junction region of the absorber layer.

The device operation can be described by identifying loss mechanisms. These can be divided into three categories. The first are optical losses that limit generation of carriers and therefore the device current. The second are recombination losses that limit

the voltage. Finally, there are parasitic losses, such as series resistance, shunt conductance, and voltage-dependent current collection, which are most evident by their effect on the fill factor but can also reduce J_{SC} and V_{OC} .

13.5.1 Light-generated Current

The highest efficiency Cu(InGa)Se₂ device has $J_{SC} = 35.2 \text{ mA/cm}^2$ [1] out of a possible 42.8 mA/cm^2 available for a band gap of 1.12 eV under AM1.5 global illumination. Quantum efficiency is a valuable tool to characterize the losses responsible for this difference in current. The light-generated current is the integral of the product of the external quantum efficiency (QE_{ext}) and the illumination spectrum. QE_{ext} is controlled by the band gap of the Cu(InGa)Se₂ absorber layer, the CdS and ZnO window layers, and a series of loss mechanisms. These losses are illustrated in Figure 13.14 where typical QE curves at two different voltage biases, 0 V and -1 V , are shown. The QE curve at -1 V is slightly higher at longer wavelengths. The current loss under 100 mW/cm^2 illumination is listed in Table 13.4 for each of these mechanisms. Losses 1 to 5 are optical and 6 is electronic. In practice, the magnitude of each of these losses will depend on the details of the device design and optical properties of the specific layers. The losses include the following:

1. Shading from a collection grid used for most devices. In an interconnected module this will be replaced by the area used for the interconnect, as discussed in Section 13.6.2.
2. Front surface reflection. On the highest-efficiency devices this is minimized with an antireflection layer for which an evaporated MgF₂ layer with thickness $\sim 100 \text{ nm}$ is commonly used. However, this is not practical in a module in which a cover glass is typically required.

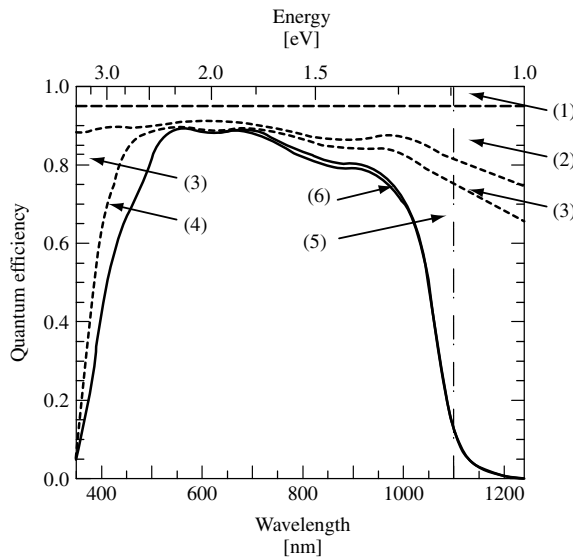


Figure 13.14 Quantum efficiency (solid lines) at 0 V and -1 V and optical losses for a Cu(InGa)Se₂/CdS solar cell in which the Cu(InGa)Se₂ has $E_g = 1.12 \text{ eV}$

Table 13.4 Current loss, ΔJ , for $E > 1.12$ eV due to the optical and collection losses illustrated in Figure 13.14 for a typical Cu(InGa)Se₂/CdS solar cell

Region in Figure 13.14	Optical loss mechanism	ΔJ [mA/cm ²]
(1)	Shading from grid with 4% area coverage	1.7
(2)	Reflection from Cu(InGa)Se ₂ /CdS/ZnO	3.8
(3)	Absorption in ZnO	1.8
(4)	Absorption in CdS	0.8
(5)	Incomplete generation in Cu(InGa)Se ₂	1.9
(6)	Incomplete collection in Cu(InGa)Se ₂	0.4

- Absorption in the TCO layer. Typically, there is 1 to 3% absorption through the visible wavelengths, which increases in the near IR region, $\lambda > 900$ nm, where free-carrier absorption becomes significant, and for $\lambda < 400$ nm near the ZnO band gap.
- Absorption in the CdS layer. This becomes appreciable at wavelengths below ~ 520 nm corresponding to the CdS band gap 2.42 eV. The loss in QE for $\lambda < 500$ nm is proportional to the CdS thickness since it is commonly assumed that electron–hole pairs generated in the CdS are not collected. Figure 13.14 shows a device with a ~ 30 nm-thick CdS layer. In practice, the CdS layer is often thicker and the absorption loss greater.
- Incomplete absorption in the Cu(InGa)Se₂ layer near the Cu(InGa)Se₂ band gap. Band gap gradients, resulting from composition gradients in many Cu(InGa)Se₂ films, also affect the steepness of the long-wavelength part of the QE curve. If the Cu(InGa)Se₂ is made thinner than ~ 1.0 μm , this loss becomes significant [163] because of insufficient absorption at long wavelengths.
- Incomplete collection of photogenerated carriers in the Cu(InGa)Se₂, discussed below.

QE_{ext} is then given by

$$QE_{\text{ext}}(\lambda, V) = [1 - R(\lambda)][1 - A_{\text{ZnO}}(\lambda)][1 - A_{\text{CdS}}(\lambda)]QE_{\text{int}}(\lambda, V) \quad (13.5)$$

where R is the total reflection, including the grid shading, A_{ZnO} is the absorption in the ZnO layer and A_{CdS} is the absorption in the CdS layer. QE_{int} , the internal quantum efficiency, is the ratio of photogenerated carriers collected to the photon flux that arrives at the absorber layer and can be approximated by [164]

$$QE_{\text{int}}(\lambda, V) \cong 1 - \frac{\exp[-\alpha(\lambda)W(V)]}{\alpha L + 1} \quad (13.6)$$

where α is the Cu(InGa)Se₂ absorption coefficient, W is the space charge width in the Cu(InGa)Se₂, and L is the minority carrier diffusion length. This approximation assumes that all carriers generated in the space charge region are collected without recombination loss. Since W is a function of the applied voltage bias, QE_{int} and total light-generated current are, in general, voltage-dependent, so the latter can be written as $J_L(V)$. Values of W in the range 0.1–0.5 μm have been reported for typical cells at 0 V.

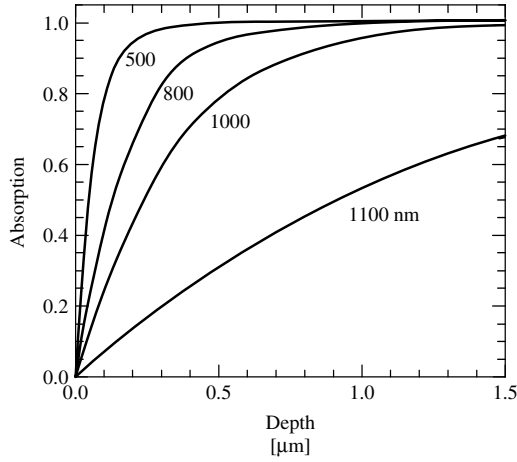


Figure 13.15 Absorption of light with different wavelengths in Cu(InGa)Se₂ with $x = 0.2$

The absorption of light with different wavelengths in Cu(InGa)Se₂ with $x = 0.2$ is shown in Figure 13.15. At thickness d , this is given by $\exp(-\alpha d)$ with α calculated at each wavelength using equation (13.3) and the data in Figure 13.6. If the effective collection length $L + W$ is smaller than 0.5 to 1 μm , a significant fraction of electrons are generated deeper into the Cu(InGa)Se₂ layer, and their incomplete collection can be a significant loss mechanism for Cu(InGa)Se₂ devices [116, 165]. The effect of $J_L(V)$ on current–voltage behavior increases with forward voltage bias and therefore has its largest effect on the fill factor and V_{OC} [166, 167]. The effect of a voltage-dependent collection on J_{SC} is illustrated in Figure 13.14 by the increase in QE measured at -1 V applied voltage bias compared to that measured at 0 V.

13.5.2 Recombination

The current–voltage (J – V) behavior of Cu(InGa)Se₂/CdS devices can be described by a general diode equation:

$$J = J_D - J_L = J_O \exp \left[\frac{q}{AkT} (V - R_S J) \right] + GV - J_L \quad (13.7)$$

with the diode current J_O given by:

$$J_O = J_{OO} \exp \left(-\frac{\Phi_b}{AkT} \right) \quad (13.8)$$

The ideality factor A , barrier height Φ_b , and prefactor J_{OO} depend on the specific recombination mechanism that dominates J_O , while the series resistance R_S and shunt conductance G are losses that occur in series or parallel with the primary diode. General expressions for A , Φ_b , and J_{OO} in the cases of recombination through the interface, space charge region, or bulk of the absorber layer can be found in various textbooks (see, for example [168]).

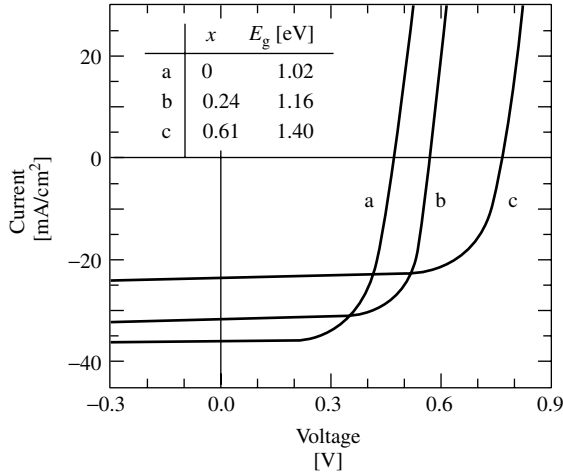


Figure 13.16 Current–voltage curves for Cu(InGa)Se₂/CdS solar cells with different relative Ga content giving (a) $E_g = 1.02$, (b) 1.16, and (c) 1.4 eV

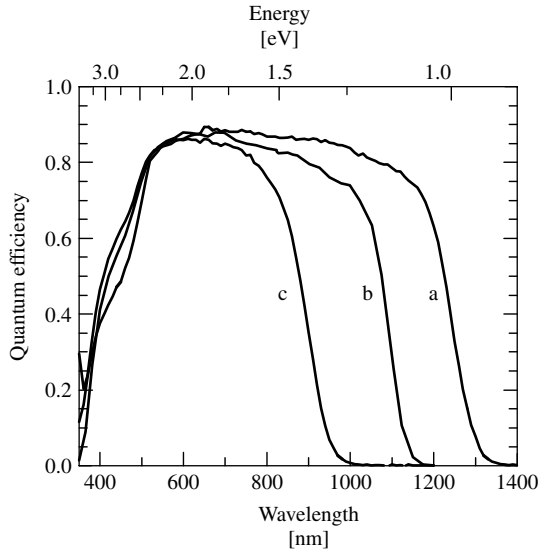


Figure 13.17 Quantum efficiency curves for the devices shown in Figure 13.16

To understand the specific diode behavior of Cu(InGa)Se₂/CdS solar cells, it is instructive to look at the effect of the Cu(InGa)Se₂ band gap, varied by changing $x \equiv \text{Ga}/(\text{In} + \text{Ga})$, and temperature. Figures 13.16 and 13.17 show J – V and QE curves for 3 devices with $x = 0, 0.24$, and 0.61 , corresponding to $E_g = 1.02, 1.16$, and 1.40 eV, respectively. V_{OC} increases and the position of the long-wavelength QE edge shifts to greater energy as E_g increases. Figure 13.18 shows the temperature dependence of V_{OC} for these devices. In each case, as $T \rightarrow 0$, $V_{OC} \rightarrow E_g/q$. Thus, combining equations (13.7)

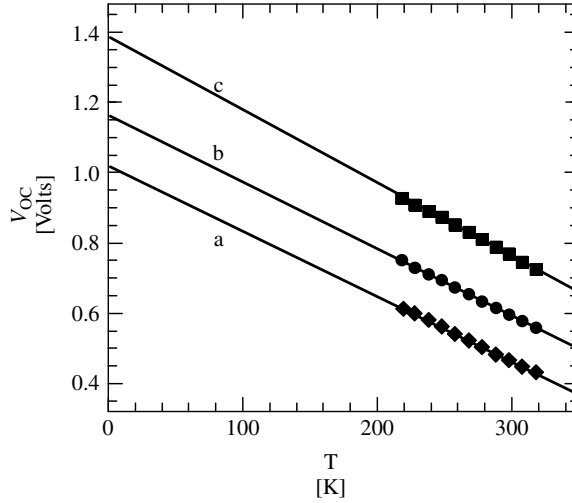


Figure 13.18 Temperature dependence of V_{OC} for the devices shown in Figure 13.16

and (13.8) and assuming $G \ll J_L/V_{OC}$, the open-circuit voltage becomes

$$V_{OC} = \frac{E_g}{q} - \frac{AkT}{q} \ln \left(\frac{J_{00}}{J_L} \right) \quad (13.9)$$

with the barrier height $\Phi_b = E_g$.

The different recombination paths are effectively connected in parallel so that V_{OC} will be controlled by the single dominant mechanism with the highest current. The values of Φ_b and A can be used to distinguish between recombination in the bulk absorber, in the space charge region of the Cu(InGa)Se_2 , or at the $\text{Cu(InGa)Se}_2/\text{CdS}$ interface [27, 169]. Each of the curves in Figure 13.16 can be fit to equation (13.7) with $A = 1.5 \pm 0.3$. For a wide range of thin-film solar cells, it has been demonstrated that $V_{OC}(T \rightarrow 0) = QE_g$ and $1 < A < 2$ similar to the data above. Specifically, this has been shown for CuInSe_2 [116, 170] and Cu(InGa)(SeS)_2 [171] devices, independent of the $(\text{CdZn})\text{S}$ buffer-layer band gap [170], and for a variety of different absorber-layer deposition processes [172]. These results for Φ_b and A indicate that $\text{Cu(InGa)Se}_2/\text{CdS}$ solar cells operate with the diode current controlled by Shockley–Read–Hall type recombination in the Cu(InGa)Se_2 layer [168]. This recombination is greatest through deep trap states in the space charge region of the Cu(InGa)Se_2 where there are comparable supplies of electrons and holes available, that is, $p \approx n$. The variation in A between 1 and 2 depends on the energies of the deep defects that act as dominant trap states [173]. As these states move toward the band edges, $A \rightarrow 1$ and the recombination becomes closer to band-to-band bulk recombination.

These observations exclude recombination in the neutral bulk region of the absorber layer, which should give $A = 1$. Interface recombination would give $\Phi_b < E_g[\text{Cu(InGa)Se}_2]$ with a dependence on the $(\text{CdZn})\text{S}$ band gap, although A might vary from 1 to >2 [174]. Back surface recombination at the Mo/Cu(InGa)Se_2 interface will

be negligible so long as the minority-carrier diffusion length is small compared to the total Cu(InGa)Se₂ thickness. If $L + W \approx d$, a back surface field may be implemented, for example, by increasing the Ga content near the Mo to give a band gap gradient.

In real Cu(InGa)Se₂ materials with imperfect structures, trap defects will not exist at discrete energies but form defect bands or tails at the valence and conduction bands. Then the total recombination current can be determined by integrating over the defect spectrum. Recombination through an exponential bandtail was used to explain the temperature dependence in A observed in some devices [175]. Analysis of the temperature dependence of A was further explained by a tunneling enhancement of the recombination current, particularly at reduced temperatures [176]. The same defects in the Cu(InGa)Se₂ space charge region that control recombination were also used to explain observed metastabilities including persistent photoconductivity and open-circuit voltage decay [177]. Admittance spectroscopy has proved to be a useful tool to characterize the distribution of electronic defects in Cu(InGa)Se₂/CdS solar cells [178] and the density of an acceptor state ~ 0.3 eV from the valence band has been correlated to V_{OC} [179]. The minority-carrier lifetime is another valuable parameter to characterize Cu(InGa)Se₂/CdS devices. Transient photocurrent [180] and time-resolved photoluminescence [167] measurements each were used to calculate lifetimes in the range of 10 to 100 ns for high-efficiency devices. Still, a critical problem that remains is to identify which of the calculated or measured defects discussed in Section 13.2 provides for the recombination traps that limit voltage in the devices. A good review of the characterization of electronic defects and their effect on Cu(InGa)Se₂ devices is provided by Rau and Schock [27].

In practice, analysis of $J-V$ data is commonly used to determine the diode parameters J_0 , A , and Φ_b . This requires that R_S and G are negligible, or suitable corrections are made to the data, and that J_L is independent of V . Failure to account for $J_L(V)$ can lead to errors in analysis of current-voltage data [166] and in many cases the fundamental diode parameters cannot be reliably determined except from $J-V$ data measured in the dark. In addition, it must be verified that there are no nonohmic effects at any contacts or junctions, which cause the appearance of a second diode for which equation (13.7) does not account. Such nonohmic behavior is often observed at reduced temperatures [170, 172]. Once it has been demonstrated that all these parasitic effects are negligible, or corrections have been made, then J_0 can be determined by a linear fit to a semilogarithmic plot of $J + J_L$ versus $V - R_S J$ and A can be determined from the slope of the derivative dV/dJ versus $1/J$ in forward bias [181], or both J_0 and A can be obtained by a least squares fit to equation (13.7). Finally, Φ_b can be determined from the temperature dependence of V_{OC} as in Figure 13.18.

It must be noted that most descriptions of transport and recombination ignore the effect of grain boundaries, implicitly assuming that grains are columnar and all transport can proceed without crossing grain boundaries. However, this is rarely, if ever, strictly true, so a comprehensive description of Cu(InGa)Se₂ solar cells must account for the possibility of recombination at grain boundaries reducing current collection or voltage. The effect of grain boundaries can be expressed as an effective diffusion length, leading to the conclusion that grain-boundary recombination is small [27]. This can occur if the grain boundaries are doped more p -type than the bulk grains so that electrons are prevented from reaching and recombining at defects in the grain boundaries [169].

13.5.3 The Cu(InGa)Se₂/CdS Interface

It may seem surprising that recombination at the Cu(InGa)Se₂/CdS interface does not limit V_{OC} since, in processing Cu(InGa)Se₂ solar cells, no special efforts are made to match lattices or reduce interface defects and the devices are typically exposed to air between the Cu(InGa)Se₂ and CdS depositions. This can be explained by type inversion of the near-junction region of the Cu(InGa)Se₂ induced by the band alignment and doping [169, 182–184]. In this case, the Fermi level at the interface is close to the conduction band so that electrons in the near surface region of the Cu(InGa)Se₂ are effectively majority carriers and there is an insufficient supply of holes available for recombination through the interface states. It has alternatively been proposed that doping due to Cd diffusion during the chemical bath deposition of CdS results in the formation of an n -type emitter and a p - n homojunction in the Cu(InGa)Se₂ [136]. This would require the junction to remain very close to the Cu(InGa)Se₂/CdS interface to minimize recombination of carriers generated near the interface, and would therefore be very process-specific.

The Cu(InGa)Se₂/CdS band diagram shown in Figure 13.19 demonstrates that the conduction-band offset ΔE_C between the CdS and the Cu(InGa)Se₂ is critical for creating the type inversion in the Cu(InGa)Se₂. In this diagram, the bulk Cu(InGa)Se₂ layer is p -type with E_g depending on the relative Ga concentration, the CdS layer is n -type with $E_g = 2.4$ eV and is totally depleted, and the bulk ZnO n^+ -layer has $E_g = 3.2$ eV. A thin HR ZnO layer between the n^+ -ZnO layer and the CdS is also assumed to be depleted. Positive ΔE_C indicates a spike in the conduction band, that is, the conduction-band minimum in the CdS is at higher energy than the conduction-band minimum of the Cu(InGa)Se₂. Figure 13.19 shows the case with $\Delta E_C = 0.3$ eV and a -0.3 eV conduction-band offset between the ZnO and the CdS [52]. Models of current transport and recombination have considered the effect of ΔE_C [184–187]. These models show that if ΔE_C is greater than about 0.5 eV, collection of photogenerated electrons in the Cu(InGa)Se₂ is impeded and

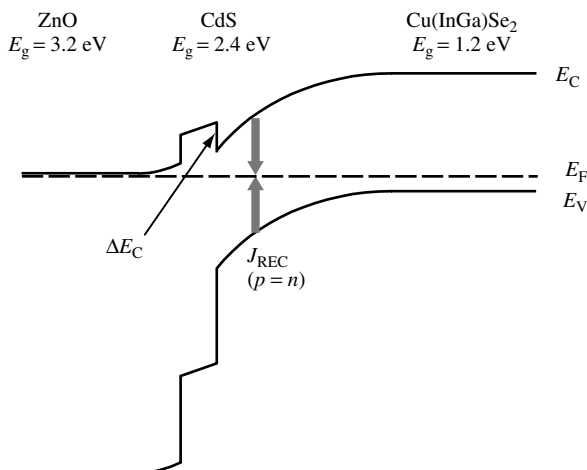


Figure 13.19 Band diagram of a ZnO/CdS/Cu(InGa)Se₂ device at 0 V in the dark. Note that the recombination current J_{REC} is greatest where $p = n$ in the space charge region of the Cu(InGa)Se₂ and not at the interface

J_{SC} or FF is reduced sharply. With a smaller spike, electrons can be transported across the interface assisted by thermionic emission [185]. On the other hand, for sufficiently negative ΔE_C the induced type inversion of the Cu(InGa)Se₂ near the interface is eliminated and interface state recombination will limit V_{OC} . An ODC layer at the surface of the absorber layer increases the band gap and primarily affects the valence band [188], so it may enhance type inversion near the junction. However, there is no convincing evidence that this layer exists in devices, so it is not shown in Figure 13.19.

Owing to its importance in the electronic behavior of Cu(InGa)Se₂/CdS devices, several efforts have been made to calculate or measure ΔE_C with varying results. Band-structure calculations gave $\Delta E_C = 0.3$ eV [189]. XPS and ultraviolet photoelectron spectroscopy (UPS) measurements of the valence band alignment indicate a positive ΔE_C between 0.2 and 0.7 eV [52, 190, 191]. These electron spectroscopy methods require ultrahigh vacuum conditions that necessitates that the CdS is deposited by vacuum evaporation. It is possible that the interface formation is different when CdS is grown by chemical bath deposition, for example, due to chemical interdiffusion, resulting in a different alignment of the conduction bands. Indirect measurements of the junction formed with chemical bath deposited CdS using a surface photovoltage technique gave $\Delta E_C = -0.1$ eV [192]. Finally, inverse photoemission spectroscopy showed that substantial chemical intermixing occurs across the interface resulting in $\Delta E_C = 0$ [193].

13.5.4 Wide and Graded Band Gap Devices

While the highest efficiency devices generally have $Ga/(In + Ga) \approx 0.1-0.3$ giving $E_g \approx 1.1-1.2$ eV, significant effort has been made to develop high-efficiency solar cells based on wider band gap alloys. This is driven primarily by the expectation that wider band gap alloys will yield higher module efficiencies due to reduced losses related to the trade-off between higher voltage and lower current at maximum power. The resulting reduction in power loss, proportional to I^2R , can be used to either (1) increase the module's active area by reducing the spacing between interconnects or (2) decrease the optical absorption in the TCO layers since they can tolerate greater resistance. Wider band gap should give a lower coefficient of temperature for the device or module output power, which will improve performance at the elevated temperatures experienced in most real terrestrial applications. Wide band gap devices could also be used as the top cell in a tandem or multijunction cell structure.

The wider band gap materials that have attracted the most attention for devices are Cu(InGa)Se₂ and CuInS₂. CuGaSe₂ has $E_g = 1.68$ eV, which is well suited for the wide band gap cell in tandem structures. CuInS₂ has $E_g = 1.53$ eV, which could be nearly optimum for a single-junction device. The highest-efficiency devices based on CuInS₂ are deposited with Cu-rich overall composition and then the excess Cu, in the form of a Cu_xS second phase, is etched away before CdS deposition [194]. Cu(InAl)Se₂ solar cells have also been considered [195]. Since CuAlSe₂ has $E_g = 2.7$ eV, the alloy requires smaller changes in relative alloy concentration and lattice parameter from CuInSe₂ than the Ga alloys to achieve comparable band gap. The highest efficiency devices of different alloys are listed in Table 13.5.

The effects of Ga incorporation on device behavior are not fully understood. The addition of a small amount of Ga to CuInSe₂ increased the open-circuit voltage even when

Table 13.5 Highest-efficiency devices for different alloy absorber layers

Material	E_g [eV]	Efficiency [%]	V_{OC} [V]	J_{SC} [mA/cm ²]	FF [%]	Reference
CuInSe ₂	1.02	15.4	515	41.2	72.6	[80]
Cu(InGa)Se ₂	1.12	18.8	678	35.2	78.6	[1]
CuGaSe ₂	1.68	8.3	861	14.2	67.9	[196]
CuInS ₂	1.53	11.4	729	21.8	71.7	[197]
Cu(InAl)Se ₂	1.16	16.9	621	36.0	75.5	[198]

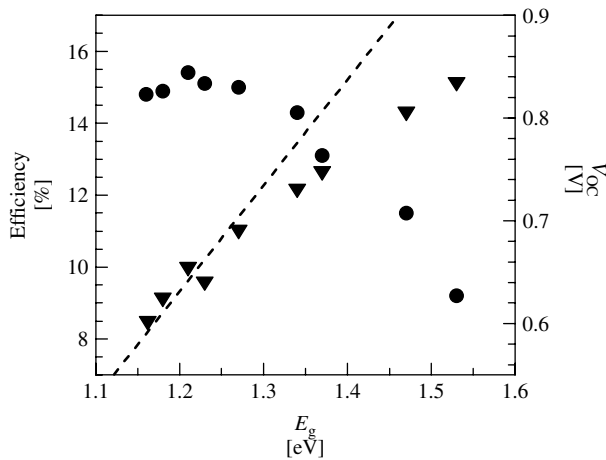


Figure 13.20 Efficiency (▼) and V_{OC} (●) as a function of Cu(InGa)Se₂ band gap, varied by increasing the relative Ga content, (From Shafarman W, Klenk R, McCandless B, *Proc. 25th IEEE Photovoltaic Specialist Conf.*, 763–768 (1996) [199]. The dashed line has slope $\Delta V_{OC}/\Delta E_g = 1$)

the Ga was confined to the back of the absorber and did not increase the band gap in the space charge region [105]. The effect of increasing band gap in Cu(InGa)Se₂/CdS solar cells on V_{OC} and efficiency is shown in Figure 13.20. Efficiency is roughly independent of band gap for $E_g < 1.3$ eV or $Ga/(In + Ga) < 0.5$ [165, 199]. With even wider band gap, V_{OC} increases to greater than 0.8 V, but the efficiency decreases. This indicates poorer electronic properties of the Cu(InGa)Se₂ absorber layer, which has two effects: voltage-dependent current collection [165], which causes the fill factor to decrease, and increased recombination [200], which reduces V_{OC} below that expected from equation (13.9) [27]. The dashed line in Figure 13.20 shows a line with slope $\Delta V_{OC}/\Delta E_g = 1$. Ideally, the increase in V_{OC} would have only a slightly smaller slope due to the dependence on J_L in the second term of equation (13.9). Admittance spectroscopy showed a correlation between the recombination and the density of a defect with an activation energy ~ 0.3 eV, which increases with E_g [200]. Transient photocapacitance measurements showed a defect band centered at 0.8 eV from the valence band, which moves closer to midgap for increasing band gap and therefore becomes more efficient as a recombination trap [201]. As the band gap becomes wider, type inversion of the absorber layer near the interface may no longer occur and interface recombination can become more significant. Analysis of both CuGaSe₂ [202] and CuInS₂ [203] solar cells showed that the low open-circuit voltages

could be caused by either space charge or interface recombination, depending on the device preparation.

Band gap gradients formed by controlled incorporation of Ga or S have been proposed as a means to increase device efficiency by separately reducing recombination and collection losses [19, 204–206]. A gradient in the conduction band from wide at the Cu(InGa)Se₂/Mo interface to narrow near the space charge region has been used to enhance minority-carrier collection [199, 206] and to reduce back surface recombination when the diffusion length is comparable to the film thickness [207]. Alternatively, a gradient from wide at the Cu(InGa)Se₂/CdS interface to narrow at the edge of the space charge region could reduce recombination and increase V_{OC} . In this case, the smaller band gap in the bulk portion of the device can still enable high optical absorption and J_{SC} [19, 206]. The most effective implementation of a surface band gap gradient may be the incorporation of S near the front surface [20] since the main effect is in lowering the valence band, instead of raising the conduction band as with Ga, and there should be less impact on collection of light-generated electrons.

13.6 MANUFACTURING ISSUES

The competitiveness of a PV technology will primarily be governed by its performance, stability, and costs. The best Cu(InGa)Se₂ cells and modules have demonstrated efficiency on a par with commercial crystalline silicon products. Long-term stability appears not to be a significant problem, as shown in field tests of prototype modules, but low-cost production remains to be demonstrated in practice.

It is evident that thin films have the potential to be produced at very low costs. Moisture barriers of aluminum films that are deposited on plastic foils to be used, for example, in potato chip bags cost less than 0.01 \$/m² to produce. This particular example is at the low end of production costs and more advanced functional coatings are in general substantially more expensive to manufacture. Thin film coatings on architectural glass cost on the order of 1 \$/m². Thus PV modules constructed from thin-film materials have the possibility for very low manufacturing costs. Whether Cu(InGa)Se₂ module production will be able to achieve this low-cost potential will depend on how well the process technology fulfills the requirements for material costs, throughput, and yield.

13.6.1 Processes and Equipment

Deposition processes can be either batch-type, in which a number of substrate plates are processed in parallel, or in-line, in which one substrate plate immediately follows the preceding one. In batch processing, a process step is completely finished before the next batch is started, whereas a substrate plate may enter an in-line process step before the previous substrate is finished in order to keep the line continuously running.

One common view on volume production is that in-line continuous processing is a prerequisite for low costs. Fabrication of large-area thin-film products with physical vapor deposition is often made in a continuous or quasi-continuous in-line system. However, the cost of a batch process can be equally low, provided the throughput is large enough. For manufacturing of Cu(InGa)Se₂ modules, this means that the CdS chemical bath deposition

can well fulfill low-cost production criteria even though it is normally a batch process. Similarly, growth of the Cu(InGa)Se_2 layer by batch selenization does not necessarily need to be associated with higher costs than Cu(InGa)Se_2 fabricated by in-line coevaporation, provided the cycle time is short enough or batch size large enough.

The commercial availability of large-area deposition systems depends on the specific process. Sputtering deposition is widely used for fabrication of large-area thin-film coatings of various kinds, for example, in the glass industry. Similar processes are used in the fabrication of most Cu(InGa)Se_2 modules for the Mo back contact and the TCO front contact, so the same type of equipment, available from a number of suppliers, can be used.

Sputtering is also typically used for deposition of the metal precursor films for fabrication of the Cu(InGa)Se_2 layer by a two-step process. The selenization step, however, requires specific custom-made process equipment. This could be selenization furnaces in which batches of plates with the precursor layers are exposed to a selenium-containing atmosphere or an in-line selenization chamber in which the plates are continuously transported through an environment with elemental selenium and substrate temperature control [208].

Elemental coevaporation of the Cu(InGa)Se_2 layer requires custom-made equipment including specially designed evaporation sources for uniform deposition of large-area substrates with accurate control. In-line evaporation using linear sources is a straightforward approach that is being developed at several laboratories and companies. An example of such a piece of equipment is illustrated in Figure 13.21.

The chemical bath deposition of CdS or Cd-free buffer layers is suitable for low-cost batch processing, in that it is a surface-controlled process that requires a limited solution volume. The equipment for dipping batches of Cu(InGa)Se_2 -coated substrate plates is relatively simple and can be custom-made. The dry buffer deposition methods under investigation have not been developed to a stage in which manufacturing is under consideration.

Chemical vapor-deposited doped ZnO as an alternative to sputtering is typically done as a batch process with a relatively small number of substrate plates deposited per

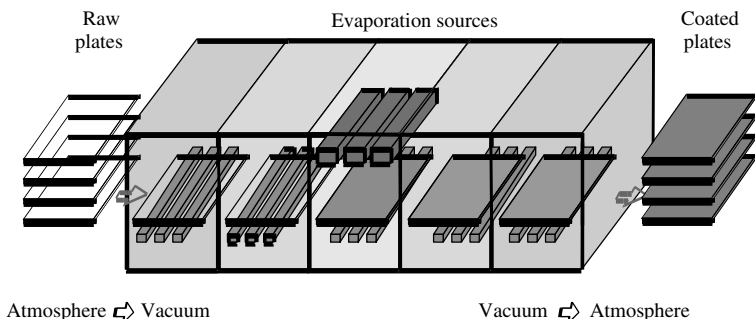


Figure 13.21 In-line coevaporation system for Cu(InGa)Se_2 with linear evaporation sources above the substrate plates and heaters below them [Courtesy of Zentrum für Sonnenenergie- und Wasserstoff-Forschung (ZSW)]. Reproduced by permission of Michael Powalla, ZSW Stuttgart, 2001

run. Throughput will eventually become an issue. However, in-line CVD processes have been developed, for example, in the manufacture of amorphous silicon solar modules.

13.6.2 Module Fabrication

Soda lime float glass is the substrate material that so far has given the best results in terms of both performance and reproducibility. It fulfills criteria on cost (3 \$/m² for 4-mm-thick glass in large volumes), smoothness, and stability, so it is well suited for commercial production. One limitation that needs to be addressed in the development of production processes is that soda lime glass starts to soften above 500°C. At the same time, the best PV properties of Cu(InGa)Se₂ are achieved at growth temperatures above 500°C. Plastic deformation due to glass softening is not acceptable in a module-production process and careful optimization of the time–temperature profile is needed to minimize the deformation.

Flexible substrate materials are attractive both for the possibility to make a lightweight flexible product with advantages for certain applications and for the possibility to deposit the thin-film materials in roll-to-roll processes, which are potentially cost-advantageous. Such roll-to-roll processing of semiconductor thin films was originally demonstrated with evaporation of CdS for solar cells [209]. The substrate materials that have shown promising results are polyimide, titanium, and steel [68, 69]. The drawbacks of polyimide are low-temperature tolerance, since the best polyimide films readily available can only withstand 400 to 450°C, and high thermal expansion. The main drawback of titanium and steel is their conductivity, which means that an electrically isolating layer is needed in order to allow monolithic series-interconnection of the cells. Such an isolation layer is not easy to make without local defects that will cause shunting of the cells. For these flexible substrate materials, sodium has to be supplied separately.

An essential cost advantage with thin-film PV modules as compared to silicon wafer-based PV modules is the possibility of monolithic interconnection. This allows modules to be fabricated directly, instead of first making cells followed by tabbing and stringing to make the series interconnection as required for silicon-wafer solar cells. A typical monolithic interconnection is illustrated schematically in Figure 13.22. The most common way to make the patterning is by using laser ablation for the Mo patterning (P1) and mechanical scribing for the two subsequent patterning steps (P2 and P3).

The final fabrication steps include attachment of electrical wires and buss bars. These are metal stripes that can be soldered, welded, or glued to contact areas near the edges of the substrate plates. Before lamination with a front cover glass, the thin-film layers are removed from the outer rim of the substrate plate in order to improve the adhesion to the lamination material, which is usually ethylene vinyl acetate (EVA). Edge sealing and framing finishes the product, but can be omitted for some applications.

13.6.3 Module Performance

The evolution of record efficiencies as reported from the certified measurement labs is displayed in Figure 13.23. The module efficiencies lag behind the cell efficiencies but follow the same basic trend. There are additional losses associated with making

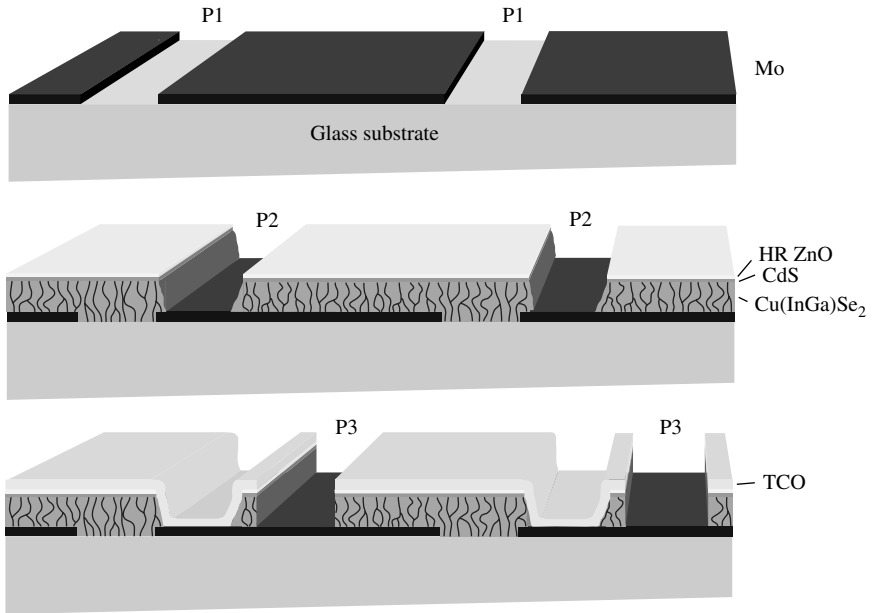


Figure 13.22 Schematic description of the manufacturing steps to make monolithic interconnections for thin-film Cu(InGa)Se₂ PV modules

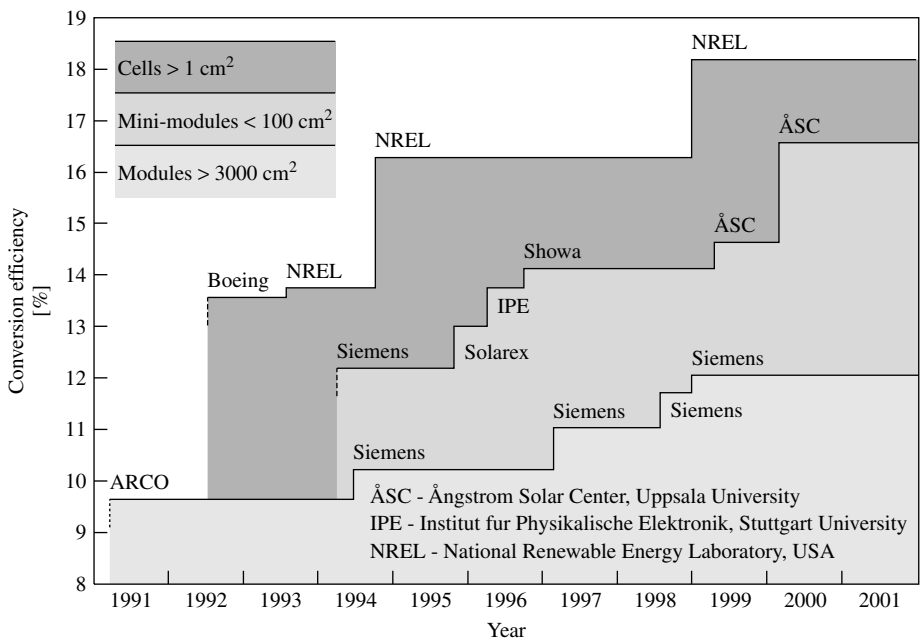


Figure 13.23 Evolution of Cu(InGa)Se₂ device record efficiencies in the past decade. All data are taken from the Solar Cell Efficiency Tables periodically published in *Progress in Photovoltaics*

series-interconnected modules instead of cells, both from series resistance and from inactive device area. In an optimized, conventional thin-film module design, these kinds of losses correspond to about 1% unit of efficiency. With a more advanced design using metal grids for interconnection, interconnect losses can be made nearly negligible [210]. Another kind of difference between modules and record cells is associated with the freedom to use higher process temperatures for cells that are not sensitive to deformed glass. These results are not necessarily relevant to module fabrication but indicate the potential of the materials.

In a product the initial efficiency is of little interest if it deteriorates after some time in operation. Cu(InGa)Se₂ modules fabricated by ARCO Solar and later Siemens Solar have shown stable performance in field tests over more than 12 years [3], as shown in Figure 13.24. On the other hand, severe degradation has been observed after exposure of cells to 85% relative humidity at 85°C for 1000 h [211], the so-called damp heat test, which is one of the certification tests in the IEC 61 646 protocol. While this test is rather severe and may not be relevant to thin-film modules, it shows the need for encapsulation techniques that minimize the exposure of the thin-film materials to moisture.

The outdoor module performance demonstrated in Figure 13.24 shows that Cu(InGa)Se₂ PV modules have the stability and performance to compete in any power application, be it stand-alone or grid-connected. Thin-film modules have a great advantage over silicon-wafer PV for consumer applications in which the power needed often is relatively small. The large substrate plates, which have a power of 40 W_P or more, can easily be cut into smaller pieces, to essentially any power specification. This is much less costly than making small crystalline-silicon modules in which each cell has to be cut into pieces before assembling the modules. Additionally, the patterning structure of the interconnects can be designed to fit a large variety of shape and voltage requirements. Aesthetically, the solid black appearance of Cu(InGa)Se₂ modules may be preferred to the nonuniform bluish appearance of the silicon-wafer modules in some building-integrated applications.

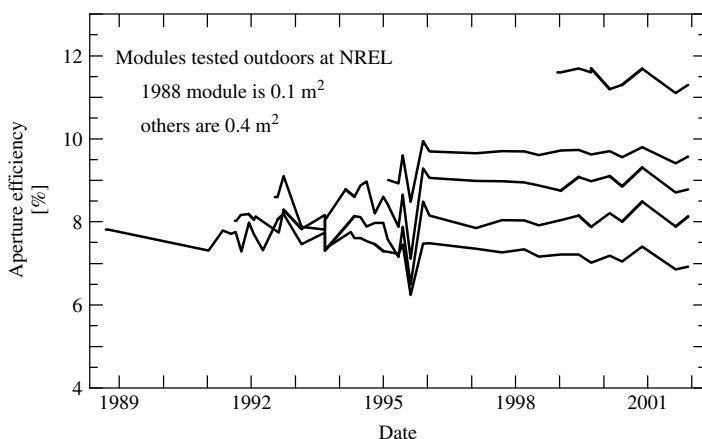


Figure 13.24 Examples of outdoor testing results at NREL of Cu(InGa)Se₂ modules showing stability over 12 years. Fluctuations in years 1992–1996 are due to changes in testing conditions. (Data courtesy of Shell Solar Industries)

Finally, for space applications, Cu(InGa)Se₂ thin-film solar cells offer potential advantages since the radiation tolerance is high as compared to crystalline-silicon solar cells [4, 5]. The potential to use a lightweight plastic substrate could lead to solar cells with very high specific power, that is, power divided by mass, which is critical for some space applications (see Chapter 10 for a more complete discussion). However, Cu(InGa)Se₂ space solar cell technology has not yet reached a commercial stage.

13.6.4 Production Costs

Material costs have direct and indirect components, and depend on the material yield of the deposition processes. The direct material costs, that is, the cost of the feedstock, will not be reduced by an increased volume of the production, depending only on the feedstock market price and how much material is needed in the film. The indirect costs, including preparation of sputtering targets or other source materials, will be reduced when production volumes are sufficiently large. The material yield, or fraction of the source material that ends up in the film, may be less than 50% for various thin-film processes. For sputtering, typically 30% of the target material ends up in the films.

In addition to materials, the other main production cost for thin-film modules is the capital cost of the equipment. To first order, any large-scale automated deposition equipment will have comparable price. Therefore, the throughput or production capacity will be very important for determining the capital cost.

Costs around 20 \$/m² for each thin-film deposition or process step may be acceptable in pilot production, but clear pathways toward costs in the range 1 to 5 \$/m² for large-volume production need to be identified. Throughput has a direct effect on cost. In an in-line process, this will depend on the substrate width and linear speed, which fundamentally depends on the deposition rate and desired thickness of the layer. If the deposition rate is relatively low, it can be compensated by having a long deposition zone in the system, for example, by having multiple targets in a sputtering system with only a relatively small increase in capital cost.

All cost advantages for thin films are lost if the production is not completed with high yield. The overall manufacturing yield can be broken down into electrical yield and mechanical yield. The electrical yield reflects the module reproducibility since it is the fraction of the modules produced which fulfill minimum performance criteria. The mechanical yield is the fraction of the substrates entering the production line that make it to the end. Mechanical losses result from broken glass substrates or malfunctioning equipment. In general, the overall yield should be well over 80%.

Another manufacturing cost is the energy usage. The energy payback time for Cu(InGa)Se₂ modules is expected to be fairly low; four months has been estimated by Alsema and van Engelenburg [212], compared to three years for crystalline-silicon modules [213].

Production-cost analyses result in a range of projected manufacturing costs. There are predictions of 1.5 to 2 \$/W_p for first-generation Cu(InGa)Se₂ plants with a few MW_p yearly capacity and projected costs of 0.4 to 0.6 \$/W_p for large-volume manufacturing [214, 215].

13.6.5 Environmental Concerns

One of the environmental issues related to the materials in Cu(InGa)Se₂ modules is the availability of less common elements. The content of the critical materials in grams per kW_P has been calculated assuming 12% module efficiency and the result is compared with the amount refined annually in Table 13.6 [216]. The fourth column expresses how much module power could be obtained from the amount refined annually and the last column shows a similar calculation based on the reserves of the various elements. Owing to uncertainties in estimates of reserves, or maximum resources, Table 13.6 just gives an indication of where, and at what level, potential problems in material supply may occur. It is clear that In is the potential bottleneck as regards primary material supply.

CuInSe₂ toxicity has been studied by administering it to rats [217]. Even at high doses negligible effects were detected. A lowest observed adverse effect level (LOAEL) of 8.3 µg/kg/day for humans was derived from these studies.

The other substances that constitute Cu(InGa)Se₂ modules are largely nontoxic except for Cd. Many aspects of its use in PV manufacturing have been studied by Fthenakis and Moskowitz [218]. Chemical bath deposition of CdS is the process step that presents the greatest health concerns due to the use of Cd, thiourea, and the generation of waste solutions. In electrodeposition of CdTe, which also is a wet process using Cd precursors, it was found that the greatest health hazards from Cd are from dust generated during feedstock preparation and from fine particles near the baths [218]. Biological monitoring at a process station showed that exposures can be maintained at a level that presents no risk to workers. Thiourea is a toxic and carcinogenic substance that also presents an exposure risk. Rinse water and dilute solutions of acids and Cd-compounds can be treated by a two-stage precipitation/ion exchange process. The Cd can be removed, and recycled, down to 1 to 10 ppb levels [218].

Most Cu(InGa)Se₂ processes use elemental Se, but the forms that are handled are solid shots or pellets that give off very little dust that could be inhaled. Elemental Se is considered to have a relatively low biological activity, but many compounds are very

Table 13.6 Critical materials in Cu(InGa)Se₂ modules with respect to primary supply (After Andersson B, Azar C, Holmberg J, Karlsson S, *Energy* **5**, 407–411 (1998) [216])

Element	Material content [g/kW _P]	Amount refined [kton/y]	Amount refined/ content [GW _P /y]	Reserves/ content [TW _P]
Mo	42	110	2600	130
Cu	17	9000	529 000	30 000
In	23	0.13	5.7	0.1
Ga	5	0.06	12	2.2
Se	43	2	46	1.9
Cd	1.6	20	12 500	330
Zn	37	7400	200 000	4100

active and highly toxic. In particular, hydrogen selenide, a gas used in some selenization processes, is extremely toxic with an “immediately dangerous to life and health” (IDLH) value of only 2 ppm [218].

There are also environmental concerns for the hazards during the operation of Cu(InGa)Se₂ modules with one potential risk being the leaching of critical materials into rainwater. This only happens if a module is broken or crushed, so the normally well-encapsulated active layers are exposed. An experimental study of the emissions of toxic elements into rainwater from crushed CuInSe₂ modules and into soil exposed to the water concluded that no acute danger to humans or the environment is likely to occur [219]. The main hazard during the active life of the CuInSe₂ modules is related to fire accidents. A study of the potential risks associated with fires in PV power plants shows that they are very limited [220]. A fire in a commercial-size system could result in harmful concentrations up to 300 m downwind of the fire if most of the CuInSe₂ materials are released. With release of 10% of the CuInSe₂ materials, concentrations were not harmful even under worst-possible meteorological conditions. The study concluded that there are no immediate risks to the public from fires in sites with CuInSe₂ modules.

Concerns for disposal of Cu(InGa)Se₂ have also been tested with respect to leachability. Zn, Mo, and Se are eluted in the highest amounts. On the basis of landfill criteria, CuInSe₂ modules will pass requirements in both Germany and the United States [217]. Because of the low volume and leaching rates of critical elements from CuInSe₂ modules, they will not be classified as hazardous waste according to most US regulations [221].

The evolution of environmental regulations, disposal options, and economics makes recycling increasingly important. In large-scale use of Cu(InGa)Se₂ modules, the supply of rare elements, in particular indium, but also selenium and gallium, provides a further motivation for recycling. The cost of recycling may be favorably offset if module materials can be reclaimed. In particular, if the glass sheets can be salvaged and reused, there will be a net gain associated with the recycling procedure. Thus, recycling may be an important consideration in the choice of encapsulation method. Double glass structures are functional and may reduce the release of CuInSe₂ materials during fires, but may increase the costs for recovering metals and reusing glass plates [221].

13.7 THE Cu(InGa)Se₂ OUTLOOK

Clearly, there has been tremendous progress in Cu(InGa)Se₂ solar cells as evidenced by the high module and cell efficiencies fabricated by many groups, the range of deposition and device options that have been developed, and the growing base of science and engineering knowledge of these materials and processes. There is good reason to be optimistic that cell efficiencies greater than 20% will be achieved before long and that module performance and yield will continue to improve. Still, there is a lack of understanding of many of the critical problems associated with semiconductor processing and a need to devote time and research focus at both the laboratory scale, to address fundamental issues, and on the pilot line, to address equipment and scale-up problems and to validate processes.

From their earliest development, CuInSe₂-based solar cells, along with other thin-film PV materials including Cu₂S, CdTe, and amorphous Si, attracted an interest because of their perceived potential to be manufactured at a lower cost than Si wafer-based PV.

However, after more than 25 years of research and development of CuInSe₂, manufacturing has only recently moved past the pilot-production stage and has not demonstrated any cost advantages. A fundamental question must be asked: what needs to be done to ensure that Cu(InGa)Se₂ solar cell technology reaches its potential for large-scale power generation?

Part of the answer is to address the critical need for the accelerated development of new manufacturing technology including improved deposition equipment and processes based on well-developed engineering models. Also, new diagnostic and process-control tools will have to be developed. This requires fundamental materials and device knowledge to determine what properties can be measured in a cell or module fabrication process that can act as reliable predictors of final performance. Better processes, equipment, and control based on a more solid knowledge base can directly translate to higher throughput, yield, and performance.

There is also a critical need for continued improvement in the fundamental science of the materials and devices [222, 223]. Significant improvements in efficiency will only come from increased V_{OC} so the chemical and electronic nature of the defects that limit it, and their origin, must be understood. This can contribute to a comprehensive model for the growth of Cu(InGa)Se₂, relating processing parameters to defect formation, junction formation, and device limitations. In addition, a fundamental understanding of the role of sodium and the nature of the grain boundaries and free surface needs to be developed. A greater understanding of the role of the CdS layer and the chemical bath process might enable alternative materials that do not contain cadmium and have wider band gap to be utilized with greater efficiency and reproducibility.

A second fundamental question to be asked is: what might be the breakthroughs that could lead to the next generation of thin-film Cu(InGa)Se₂-based solar cells?

Further development of wide band gap alloys to enable cells to be made with $E_g \geq 1.5$ eV without any decrease in performance will have several benefits for module fabrication and performance as discussed in Section 13.5. In addition, development of a cell with $E_g \approx 1.7$ eV is a prerequisite for tandem cells based on the polycrystalline thin films to be developed. A monolithic tandem cell has the potential to attain efficiencies of 25% or more. The CuInSe₂ alloy system is ideally suited for such a structure since a CuInSe₂ cell with $E_g = 1.0$ eV would make an ideal bottom cell with any of the alloys that increase band gap to 1.7 eV for the top cell. Even if a high-efficiency wide band gap cell is developed, such a structure will require the development of a transparent interconnect between the top and bottom cells and improvements in cell structure or low-temperature processes to allow the bottom cell to survive the subsequent processing of the top cell.

Low-temperature processing of the Cu(InGa)Se₂ layer without loss of efficiency in the final solar cell can have significant additional benefits. With lower substrate temperature, alternative substrate materials, like a flexible polymer web, can be utilized. In addition, lower T_{SS} can reduce thermally induced stress on the substrate, allowing faster heat-up and cooldown, and decrease the heat load and stress on the entire deposition system. Similarly, there may be significant cost and processing advantages to a cell structure that enables the use of a Cu(InGa)Se₂ layer much less than 1 μm .

With all these challenges to improve the fundamental knowledge behind Cu(InGa)Se₂ materials and devices and to develop new manufacturing technology and breakthrough advancements, research and development on Cu(InGa)Se₂ and related materials remains exciting and promising. All of the reasons for the initial excitement over the potential for thin-film Cu(InGa)Se₂ remain valid. The high efficiency, demonstrated stability, and tolerance to material and process variations give great hope that it will be a major contributor to our solar electric future.

REFERENCES

1. Contreras M *et al.*, *Prog. Photovolt.* **7**, 311–316 (1999).
2. Tanaka *et al.*, *Proc. 17th Euro. Conf. Photovoltaic Solar Energy Conversion*, 989–994 (2001).
3. Wieting R, *AIP Conf. Proc.* **462**, 3–8 (1999).
4. Burgess R *et al.*, *Proc. 20th IEEE Photovoltaic Specialist Conf.*, 909–912 (1988).
5. Jasenek A *et al.*, *Thin Solid Films* **387**, 228–230 (2001).
6. Hahn H *et al.*, *Z. Anorg. Allg. Chem.* **271**, 153–170 (1953).
7. Shay J, Wernick J, *Ternary Chalcopyrite Semiconductors: Growth, Electronic Properties, and Application*, Pergamon Press, Oxford (1974).
8. Tell B, Shay J, Kasper H, *Phys. Rev.* **B4**, 4455–4459 (1971).
9. Tell B, Shay J, Kasper H, *J. Appl. Phys.* **43**, 2469, 2470 (1972).
10. Wagner S, Shay J, Migliorato P, Kasper H, *Appl. Phys. Lett.* **25**, 434, 435 (1974).
11. Shay J, Wagner S, Kasper H, *Appl. Phys. Lett.* **27**, 89–90 (1975).
12. Meakin J, *Proc. SPIE Conf. 543: Photovoltaics*, 108–118 (1985).
13. Kazmerski L, White F, Morgan G, *Appl. Phys. Lett.* **29**, 268, 269 (1976).
14. Mickelsen R, Chen W, *Proc. 15th IEEE Photovoltaic Specialist Conf.*, 800–804 (1981).
15. Mickelsen R, Chen W, *Proc. 16th IEEE Photovoltaic Specialist Conf.*, 781–785 (1982).
16. Chen W *et al.*, *Proc. 19th IEEE Photovoltaic Specialist Conf.*, 1445–1447 (1987).
17. Potter R, *Sol. Cells* **16**, 521–527 (1986).
18. Hedström J *et al.*, *Proc. 23rd IEEE Photovoltaic Specialist Conf.*, 364–371 (1993).
19. Gabor A *et al.*, *Sol. Energy Mater. Sol. Cells* **4**, 247–260 (1996).
20. Tarrant D, Ermer J, *Proc. 23rd IEEE Photovoltaic Specialist Conf.*, 372–375 (1993).
21. Rocheleau R, Meakin J, Birkmire R, *Proc. 19th IEEE Photovoltaic Specialist Conf.*, 972–976 (1987).
22. Mitchell K *et al.*, *IEEE Trans. Electron. Devices* **37**, 410–417 (1990).
23. Kazmerski L, Wagner S, “Cu-Ternary Chalcopyrite Solar Cells”, in Coutts T, Meakin J, Eds, *Current Topics in Photovoltaics*, 41–109, Academic Press, London (1985).
24. Haneman D, *Crit. Rev. Solid State Mater. Sci.* **14**, 377–413 (1988).
25. Rockett A, Birkmire R, *J. Appl. Phys.* **70**, R81–R97 (1991).
26. Rockett A, Bodegård M, Granath K, Stolt L, *Proc. 25th IEEE Photovoltaic Specialist Conf.*, 985–987 (1996).
27. Rau U, Schock H, *Appl. Phys. A* **69**, 131–147 (1999).
28. Suri D, Nagpal K, Chadha G, *J. Appl. Crystallogr.* **22**, 578 (1989) (JCPDS 40-1487).
29. Ciszek T, *J. Cryst. Growth.* **70**, 405–410 (1984).
30. Neumann H, *Sol. Cells* **16**, 317–333 (1986).
31. Wasim S, *Sol. Cells* **16**, 289–316 (1986).
32. Gödecke T, Haalboom T, Ernst F, *Z. Metallkd.* **91**, 622–634 (2000).
33. Ye J, Yoshida T, Nakamura Y, Nittono O, *Jpn. J. Appl. Phys.* **35**, 395–400 (1996).
34. Zhang S, Wei S, Zunger A, *Phys. Rev. Lett.* **78**, 4059–4062 (1997).
35. Herberholz R *et al.*, *Eur. Phys. J.* **6**, 131–139 (1999).
36. Wei S, Zhang S, Zunger A, *Appl. Phys. Lett.* **72**, 3199–3201 (1998).

37. Schroeder D, Rockett A, *J. Appl. Phys.* **82**, 4982–4985 (1997).
38. Wei S, Zhang S, Zunger A, *J. Appl. Phys.* **85**, 7214–7218 (1999).
39. Ruckh M *et al.*, *Sol. Energy Mater. Sol. Cells* **41/42**, 335–343 (1996).
40. Kazmerski L *et al.*, *J. Vac. Sci. Technol., A* **1**, 395–398 (1983).
41. Rincón C, González J, *Sol. Cells* **16**, 357–362 (1986).
42. Alonso M *et al.*, *Phys. Rev. B* **63**, 075203 1–13 (2001).
43. Alonso M *et al.*, *Appl. Phys. A* **74**, 659–664 (2002).
44. Wei S, Zunger A, *Appl. Phys. Lett.* **72**, 2011–2013 (1998).
45. Noufi R, Axton R, Herrington C, Deb S, *Appl. Phys. Lett.* **45**, 668–670 (1984).
46. Neumann H, Tomlinson R, *Sol. Cells* **28**, 301–313 (1990).
47. Zhang S, Wei S, Zunger A, Katayama-Yoshida H, *Phys. Rev. B* **57**, 9642–9656 (1998).
48. Schroeder D, Hernandez J, Berry G, Rockett A, *J. Appl. Phys.* **72**, 749–752 (1998).
49. Kiely C, Pond R, Kenshole G, Rockett A, *Philos. Mag. A* **63**, 2149–2173 (1991).
50. Chen J *et al.*, *Thin Solid Films* **219**, 183–192 (1992).
51. Wada T, *Sol. Energy Mater. Sol. Cells* **49**, 249–260 (1997).
52. Schmid D, Ruckh M, Grunwald F, Schock H, *J. Appl. Phys.* **73**, 2902–2909 (1993).
53. Gartsman K *et al.*, *J. Appl. Phys.* **82**, 4282–4285 (1997).
54. Kylvner A, *J. Electrochem. Soc.* **146**, 1816–1823 (1999).
55. Scheer R, *Trends Vac. Sci. Tech.* **2**, 77–112 (1997).
56. Damaskinos S, Meakin J, Phillips J, *Proc. 19th IEEE Photovoltaic Specialist Conf.*, 1299–1304 (1987).
57. Cahen D, Noufi R, *Appl. Phys. Lett.* **54**, 558–560 (1989).
58. Kronik L, Cahen D, Schock H, *Adv. Mater.* **10**, 31–36 (1998).
59. Niles D, Al-Jassim M, Ramanathan K, *J. Vac. Sci. Technol., A* **17**, 291–296 (1999).
60. Bodegård M, Stolt L, Hedström J, *Proc. 12th Euro. Conf. Photovoltaic Solar Energy Conversion*, 1743–1746 (1994).
61. Bodegård M, Granath K, Rockett A, Stolt L, *Sol. Energy Mater. Sol. Cells* **58**, 199–208 (1999).
62. Shafarman W *et al.*, *AIP Conf. Proc.* **394**, 123–131 (1997).
63. Contreras M *et al.*, *Thin Solid Films* **361–2**, 167–171 (2000).
64. Boyd D, Thompson D, Kirk-Othmer *Encyclopaedia of Chemical Technology*, Vol. 11, 3rd Edition, 807–880, John Wiley (1980).
65. Probst V *et al.*, *Proc. 1st World Conf. Photovoltaic Solar Energy Conversion*, 144–147 (1994).
66. Contreras M *et al.*, *Proc. 26th IEEE Photovoltaic Specialist Conf.*, 359–362 (1997).
67. Jensen C, Wieting R, *Proc. 13th Euro. Conf. Photovoltaic Solar Energy Conversion*, 1631–1633 (1995).
68. Basol B, Kapur V, Leidholm C, Halani A, *Proc. 25th IEEE Photovoltaic Specialist Conf.*, 157–162 (1996).
69. Hartmann M *et al.*, *Proc. 28th IEEE Photovoltaic Specialist Conf.*, 638–641 (2000).
70. Vink T, Somers M, Daams J, Dirks A, *J. Appl. Phys.* **70**, 4301–4308 (1991).
71. Wada T, Kohara N, Nishiwaki S, Negami T, *Thin Solid Films* **387**, 118–122 (2001).
72. Matson R *et al.*, *Sol. Cells* **11**, 301–305 (1984).
73. Mattox D, *Handbook of Physical Vapor Deposition (PVD) Processing*, Noyes Publ., Park Ridge, NJ (1998).
74. Jackson S, Baron B, Rocheleau R, Russell T, *Am. Inst. Chem. Eng. J.* **33**, 711–720 (1987).
75. Shafarman W, Zhu J, *Thin Solid Films* **361–2**, 473–477 (2000).
76. Klenk R, Walter T, Schock H, Cahen D, *Adv. Mater.* **5**, 114–119 (1993).
77. Kessler J *et al.*, *Proc. 12th Euro. Conf. Photovoltaic Solar Energy Conversion*, 648–652 (1994).
78. Gabor A *et al.*, *Appl. Phys. Lett.* **65**, 198–200 (1994).
79. Hasoon F *et al.*, *Thin Solid Films* **387**, 1–5 (2001).
80. Stolt L *et al.*, *Appl. Phys. Lett.* **62**, 597–599 (1993).

81. Stolt L, Hedström J, Sigurd D, *J. Vac. Sci. Technol.* **A3**, 403–407 (1985).
82. Powalla M, Voorwinden G, Dimmler B, *Proc. 14th Euro. Conf. Photovoltaic Solar Energy Conversion*, 1270–1273 (1997).
83. Eisgruber I *et al.*, *Proc. 28th IEEE Photovoltaic Specialist Conf.*, 505–508 (2000).
84. Nishitani M, Negami T, Wada T, *Thin Solid Films* **258**, 313–316 (1995).
85. Negami T *et al.*, *Mater. Res. Soc. Symp.* **426**, 267–278 (1996).
86. Grindle S, Smith C, Mittleman S, *Appl. Phys. Lett.* **35**, 24–26 (1979).
87. Chu T, Chu S, Lin S, Yue J, *J. Electrochem. Soc.* **131**, 2182–2185 (1984).
88. Gay R *et al.*, *Proc. 12th Euro. Conf. Photovoltaic Solar Energy Conversion*, 935–938 (1994).
89. Kapur V, Basol B, Tseng E, *Sol. Cells* **21**, 65–70 (1987).
90. Basol B, Kapur V, *IEEE Trans. Electron. Devices* **37**, 418–421 (1990).
91. Garcia F, Tomar M, *Jpn. J. Appl. Phys.* **22S**, 535–540 (1983).
92. Schulz D *et al.*, *Proc. 27th IEEE Photovoltaic Specialist Conf.*, 483–486 (1997).
93. Knowles A, Oumous H, Carter M, Hill R, *Semicond. Sci. Technol.* **3**, 1143, 1144 (1988).
94. Nadenau V *et al.*, *Prog. Photovolt.* **3**, 363–382 (1995).
95. Pern F *et al.*, *Sol. Cells* **24**, 81–90 (1988).
96. Guillemoles J *et al.*, *J. Appl. Phys.* **79**, 7293–7302 (1996).
97. Sato H *et al.*, *Proc. 23rd IEEE Photovoltaic Specialist Conf.*, 521–526 (1993).
98. Kessler J, Ditttrich H, Grunwald F, Schock H, *Proc. 10th Euro. Conf. Photovoltaic Solar Energy Conversion*, 879–882 (1991).
99. Oumous H *et al.*, *Proc. 9th Euro. Conf. Photovoltaic Solar Energy Conversion*, 153–156 (1992).
100. Karg F *et al.*, *Proc. 23rd IEEE Photovoltaic Specialist Conf.*, 441–446 (1993).
101. Mooney G *et al.*, *Appl. Phys. Lett.* **58**, 2678–2680 (1991).
102. Verma S, Orbey N, Birkmire R, Russell T, *Prog. Photovolt.* **4**, 341–353 (1996).
103. Wolf D, Müller G, *Thin Solid Films* **361–2**, 155–161 (2000).
104. Orbey N, Norsworthy G, Birkmire R, Russell T, *Prog. Photovolt.* **6**, 79–86 (1998).
105. Jensen C, Tarrant D, Ermer J, Pollock G, *Proc. 23rd IEEE Photovoltaic Specialist Conf.*, 577–580 (1993).
106. Marudachalam M *et al.*, *Appl. Phys. Lett.* **67**, 3978–3980 (1995).
107. Kushiya K *et al.*, *Proc. 25th IEEE Photovoltaic Specialist Conf.*, 989–993 (1995).
108. Thornton J, Lomasson T, Talieh H, Tseng B, *Sol. Cells* **24**, 1–9 (1988).
109. Talieh H, Rockett A, *Sol. Cells* **27**, 321–329 (1989).
110. Guenoun K, Djessas K, Massé G, *J. Appl. Phys.* **84**, 589–595 (1998).
111. Murali K, *Thin Solid Films* **167**, L19–L22 (1988).
112. Galindo H *et al.*, *Thin Solid Films* **170**, 227–234 (1989).
113. Abernathy C *et al.*, *Appl. Phys. Lett.* **45**, 890 (1984).
114. Kazmerski L, Ireland P, White F, Cooper R, *Proc. 13th IEEE Photovoltaic Specialist Conf.*, 184–189 (1978).
115. Potter R, Eberspacher C, Fabick L, *Proc. 18th IEEE Photovoltaic Specialist Conf.*, 1659–1664 (1985).
116. Mitchell K, Liu H, *Proc. 20th IEEE Photovoltaic Specialist Conf.*, 1461–1468 (1988).
117. Cashman R, *J. Opt. Soc. Am.* **36**, 356 (1946).
118. Kitaev G, Uritskaya A, Mokrushin S, *Sov. J. Phys. Chem.* **39**, 1101 (1965).
119. Kainthla R, Pandya D, Chopra K, *J. Electrochem. Soc.* **127**, 277–283 (1980).
120. Kaur I, Pandya D, Chopra K, *J. Electrochem. Soc.* **127**, 943–948 (1980).
121. Lincot D, Ortega-Borges R, *J. Electrochem. Soc.* **139**, 1880–1889 (1992).
122. Lincot D, Ortega-Borges R, Froment M, *Philos. Mag. B* **68**, 185–194 (1993).
123. Nakada T, Kunioka A, *Appl. Phys. Lett.* **74**, 2444–2446 (1999).
124. Kylner A, Rockett A, Stolt L, *Solid State Phen.* **51–52**, 533–539 (1996).
125. Hashimoto Y *et al.*, *Sol. Energy Mater. Sol. Cells* **50**, 71–77 (1998).
126. Kylner A, Lindgren J, Stolt L, *J. Electrochem. Soc.* **143**, 2662–2669 (1996).

127. Kylner A, Niemi E, *Proc. 14th Euro. Conf. Photovoltaic Solar Energy Conversion*, 1321–1326 (1997).
128. Cherin P, Lind E, Davis E, *J. Electrochem. Soc.* **117**, 233–236 (1970).
129. Grzeta-Plenkovic B, Popovic S, Celustka B, Santic B, *J. Appl. Crystallogr.* **13**, 311–315 (1980).
130. Kessler J *et al.*, *Tech. Digest PVSEC-6*, 1005–1010 (1992).
131. Yu P, Faile S, Park Y, *Appl. Phys. Lett.* **26**, 384, 385 (1975).
132. Tell B, Wagner S, Bridenbaugh P, *Appl. Phys. Lett.* **28**, 454, 455 (1976).
133. Kazmerski L, Jamjoum O, Ireland P, *J. Vac. Sci. Technol.* **21**, 486–490 (1982).
134. Heske C *et al.*, *Appl. Phys. Lett.* **74**, 1451–1453 (1999).
135. Kylner A, *J. Electrochem. Soc.* **143**, 1816–1823 (1999).
136. Ramanathan K *et al.*, *Proc. 2nd World Conf. Photovoltaic Solar Energy Conversion*, 477–482 (1998).
137. Wang L *et al.*, *MRS Symp.* **569**, 127–132 (1999).
138. Leskelä M, Ritala M, *Thin Solid Films* **409**, 138–146 (2002).
139. Kessler J *et al.*, *Proc. 23rd IEEE Photovoltaic Specialist Conf.*, 447–452 (1993).
140. Olsen L *et al.*, *Proc. 26th IEEE Photovoltaic Specialist Conf.*, 363–366 (1997).
141. Sterner J, Kessler J, Bodegård M, Stolt L, *Proc. 2nd World Conf. Photovoltaic Solar Energy Conversion*, 1145–1148 (1998).
142. Bhattacharya R *et al.*, *Sol. Energy Mater. Sol. Cells* **63**, 367–374 (2000).
143. Kushiya K *et al.*, *Sol. Energy Mater. Solar Cells* **49**, 277–283 (1997).
144. Nakada T, Furumi K, Kunioka A, *Trans. Electron Devices* **46**, 2093–2097 (1999).
145. Muffler H *et al.*, *Proc. 28th IEEE Photovoltaic Specialist Conf.*, 610–613 (2000).
146. Ennaoui A, Blieske U, Lux-Steiner M, *Prog. Photovolt.* **6**, 447–451 (1998).
147. Othake Y, Kushiya K, Yamada A, Konagai M, *Proc. 1st World Conf. Photovoltaic Solar Energy Conversion*, 218–221 (1994).
148. Engelhardt F *et al.*, *Proc. 2nd World Conf. Photovoltaic Solar Energy Conversion* (1998).
149. Othake Y *et al.*, *Proc. 25th IEEE Photovoltaic Specialist Conf.*, 793–796 (1996).
150. Othake Y *et al.*, *Sol. Energy Mater. Sol. Cells* **49**, 269–275 (1997).
151. Hariskos D *et al.*, *Proc. 13th Euro. Conf. Photovoltaic Solar Energy Conversion*, 1995–1998 (1995).
152. Guillemoles J *et al.*, *Jpn. J. Appl. Phys.* **40**, 6065–6068 (2001).
153. Gordon R, *MRS Bull.* **25**, 52–57 (2000).
154. Lewis B, Paine D, *MRS Bull.* **25**, 22–27 (2000).
155. Menner R, Schäffler R, Sprecher B, Dimmler B, *Proc. 2nd World Conf. Photovoltaic Solar Energy Conversion*, 660–663 (1998).
156. Ruckh M *et al.*, *Proc. 25th IEEE Photovoltaic Specialist Conf.*, 825–828 (1996).
157. Westwood W, “Reactive Sputter Deposition”, in Rosnagel S, Cuomo J, Westwood W, Eds, *Handbook of Plasma Processing Technology*, Chap. 9, Noyes Publ., Park Ridge, NJ (1990).
158. Tarrant D, Gay R, *Proc. 2001 NCPV Prog. Rev. Meeting*, 113–114 (Nov. 2001).
159. Stolt L, Hedström J, Skarp J, *Proc. 1st World Conf. Photovoltaic Solar Energy Conversion*, 250–253 (1994).
160. Rau U, Schmidt M, *Thin Solid Films* **387**, 141–146 (2001).
161. Kessler J *et al.*, *Proc. 16th Euro. Conf. Photovoltaic Solar Energy Conversion*, 775–778 (2000).
162. Cooray N, Kushiya K, Fujimaki A, Okumura D, *Jpn. J. Appl. Phys.* **38**, 6213–6218 (1999).
163. Lundberg O, Bodegård M, Malmström J, Stolt L, *Prog. Photovolt.* **11** (2002).
164. Fahrenbruch A, Bube R, *Fundamentals of Solar Cells*, 231–234, Academic Press, New York (1983).
165. Shafarman W, Klenk R, McCandless B, *J. Appl. Phys.* **79**, 7324–7328 (1996).
166. Eron M, Rothwarf A, *Appl. Phys. Lett.* **44**, 131 (1984).
167. Ohnesorge B *et al.*, *Appl. Phys. Lett.* **73**, 1224–1227 (1998).

168. Fahrenbruch A, Bube R, *Fundamentals of Solar Cells*, 105–161, Academic Press, New York (1983).
169. Phillips J *et al.*, *Phys. Status Solidi B* **194**, 31–39 (1996).
170. Roy M, Damaskinos S, Phillips J, *Proc. 20th IEEE Photovoltaic Specialist Conf.*, 1618–1623 (1988).
171. Walter T, Menner R, Köble C, Schock H, *Proc. 12th Euro. Conf. Photovoltaic Solar Energy Conversion*, 1755–1758 (1994).
172. Shafarman W, Phillips J, *Proc. 23rd IEEE Photovoltaic Specialist Conf.*, 364–369 (1993).
173. Sah C, Noyce R, Shockley W, *Proc. Inst. Radio Engrs.* **45**, 1228–1243 (1957).
174. Eron M, Rothwarf A, *J. Appl. Phys.* **57**, 2275–2279 (1985).
175. Walter T, Herberholz R, Schock H, *Solid State Phen.* **51**, 301–316 (1996).
176. Rau U, *Appl. Phys. Lett.* **74**, 111–113 (1999).
177. Meyer T *et al.*, *Eur. J. Appl. Phys.* **8**, 43–52 (1999).
178. Walter T, Herberholz R, Müller C, Schock H, *J. Appl. Phys.* **80**, 4411–4420 (1996).
179. Herberholz R *et al.*, *Proc. 14th Euro. Conf. Photovoltaic Solar Energy Conversion*, 1246–1249 (1997).
180. Nishitani M, Negami T, Kohara N, Wada T, *J. Appl. Phys.* **82**, 3572–3575 (1997).
181. Sites J, Mauk P, *Sol. Cells* **27**, 411–417 (1987).
182. Turner G, Schwartz R, Gray J, *Proc. 20th IEEE Photovoltaic Specialist Conf.*, 1457–1460 (1988).
183. Schwartz R, Gray J, Lee Y, *Proc. 22nd IEEE Photovoltaic Specialist Conf.*, 920–923 (1991).
184. Klenk R, *Thin Solid Films* **387**, 135–140 (2001).
185. Niemegeers A, Burgelman M, De Vos A, *Appl. Phys. Lett.* **67**, 843–845 (1995).
186. Liu X, Sites J, *AIP Conf. Proc.* **353**, 444–453 (1996).
187. Minemoto T *et al.*, *Thin Solid Films* **67**, 83–88 (2001).
188. Schmid D, Ruckh M, Schock H, *Sol. Energy Mater. Sol. Cells* **41–2**, 281–294 (1996).
189. Wei S, Zunger A, *Appl. Phys. Lett.* **63**, 2549–2551 (1993).
190. Nelson A *et al.*, *Phys. Rev. B* **42**, 7518–7523 (1990).
191. Löher T, Jaegermann W, Pettenkofer C, *J. Appl. Phys.* **77**, 731–738 (1995).
192. Kronik L *et al.*, *Appl. Phys. Lett.* **67**, 1405–1407 (1995).
193. Morkel M *et al.*, *Appl. Phys. Lett.* **79**, 4482–4485 (2001).
194. Scheer R *et al.*, *Appl. Phys. Lett.* **63**, 3294–3296 (1993).
195. Paulson P *et al.*, *J. Appl. Phys.* **91**, 10153–10156 (2002).
196. Nadenau V, Hariskos D, Schock H, *Proc. 14th Euro. Conf. Photovoltaic Solar Energy Conversion*, 1250–1253 (1997).
197. Siemer K *et al.*, *Sol. Energy Mater. Sol. Cells* **67**, 159–166 (2001).
198. Marsillac S *et al.*, *Appl. Phys. Lett.* **81**, 1350–1352 (2002).
199. Shafarman W, Klenk R, McCandless B, *Proc. 25th IEEE Photovoltaic Specialist Conf.*, 763–768 (1996).
200. Hanna G, Jasenek A, Rau U, Schock H, *Thin Solid Films* **387**, 71–73 (2001).
201. Heath J *et al.*, *Appl. Phys. Lett.* **80**, 4540 (2002).
202. Nadenau V, Jasenek A, Rau U, Schock H, *J. Appl. Phys.* **87**, 584–593 (2000).
203. Hengel I, Neisser A, Klenk R, Lux-Steiner M, *Thin Solid Films* **361–2**, 458–462 (2000).
204. Gray J, Lee Y, *Proc. 1st World Conf. Photovoltaic Solar Energy Conversion*, 123–126 (1994).
205. Topic M, Smole F, Furlan J, *J. Appl. Phys.* **79**, 8537–8540 (1996).
206. Dullweber T, Hanna G, Rau U, Schock H, *Sol. Energy Mater. Sol. Cells* **67**, 145–150 (2001).
207. Dullweber T *et al.*, *Thin Solid Films* **387**, 11–13 (2001).
208. Probst V *et al.*, *Thin Solid Films* **387**, 262–267 (2001).
209. Russell T *et al.*, *Proc. 15th IEEE Photovoltaic Specialist Conf.*, 743–748 (1982).
210. Kessler J, Wennerberg J, Bodegård M, Stolt L, *Sol. Energy Mater. Sol. Cells* **67**, 59–65 (2001).

211. Wennerberg J, Kessler J, Stolt L, *Proc. 16th Euro. Conf. Photovoltaic Solar Energy Conversion*, 309–312 (2000).
212. Alsema E, van Engelenburg B, *Proc. 11th Euro. Conf. Photovoltaic Solar Energy Conversion*, 995–998 (1993).
213. Jester T, *Prog. Photovolt.* **10**, 99–106 (2002).
214. Woodcock J *et al.*, *Proc. 14th Euro. Conf. Photovoltaic Solar Energy Conversion*, 857–860 (1993).
215. Zweibel K, *Sol. Energy Mater. Sol. Cells* **59**, 1–18 (1999).
216. Andersson B, Azar C, Holmberg J, Karlsson S, *Energy* **23**, 407–411 (1998).
217. Thumm W *et al.*, *Proc. 1st World Conf. Photovoltaic Solar Energy Conversion*, 262–265 (1994).
218. Fthenakis V, Moskowitz P, *Prog. Photovolt.* **3**, 295–306 (1995).
219. Steinberger H, *Prog. Photovolt.* **6**, 99–103 (1998).
220. Moskowitz P, Fthenakis V, *Sol. Cells* **29**, 63–71 (1990).
221. Eberspacher C, Fthenakis V, *Proc. 26th IEEE Photovoltaic Specialist Conf.*, 1067–1072 (1997).
222. Schock H, Noufi R, *Prog. Photovolt.* **8**, 151–160 (2000).
223. Birkmire R, *Proc. 26th IEEE Photovoltaic Specialist Conf.*, 295–300 (1997).